

# Diagnostic line ratios in the IC 1805 optical gas complex

Dominic Lagrois,<sup>1,2★</sup> Gilles Joncas<sup>1,2</sup> and Laurent Drissen<sup>1,2</sup>

<sup>1</sup>*Département de Physique, de Génie Physique et d'Optique, Université Laval, Québec, QC G1V 0A6, Canada*

<sup>2</sup>*Centre de Recherche en Astrophysique du Québec, Canada*

Accepted 2011 November 11. Received 2011 November 10; in original form 2011 August 29

## ABSTRACT

Large H II regions, with angular dimensions exceeding 10 pc, usually enclose numerous massive O-stars. Stellar winds from such stars are expected to play a sizeable role in the dynamical, morphological and chemical evolution of the targeted nebula. Kinematically, stellar winds remain hardly observable, i.e. the typical expansion velocities of wind-blown bubbles being often confused with other dynamical processes also regularly found H II regions. However, supersonic shock waves, developed by stellar winds, should favour shock excitation and leave a well-defined spectral signature in the ionized nebular content. In this work, the presence of stellar winds, observed through shock excitation, is investigated in the brightest portions of the Galactic IC 1805 nebula, a giant H II region encompassing at least 10 O-stars from main-sequence O9 to giant and supergiant O4. The use of the imaging Fourier transform spectrometer SpIOMM enabled the simultaneous acquisition of the spectral information associated with the H $\alpha$   $\lambda$ 6563 Å, [N II]  $\lambda$  $\lambda$ 6548, 6584 Å, and [S II]  $\lambda$  $\lambda$ 6716, 6731 Å ionic lines. Diagnostic diagrams, first introduced by Sabbadin and collaborators, were used to circumscribe portions of the nebula likely subject to shock excitation from other areas dominated by photoionization. The gas compression, expected from supersonic shocks, is investigated by comparing the pre- and post-shocked material's densities computed from the [S II]  $\lambda$ 6716/[S II]  $\lambda$ 6731 line ratio. The typical [N II]  $\lambda$ 6584/[N II]  $\lambda$ 6548 line ratio slightly exceeds the theoretical value of 3 expected in low-density regimes. To explain such behaviour, a scenario based on collisional de-excitations affecting the [N II]  $\lambda$ 6548 Å line is proposed.

**Key words:** techniques: spectroscopic – H II regions – ISM: individual objects: IC 1805 – ISM: lines and bands.

## 1 INTRODUCTION

The presence of ionized material in the interstellar medium (ISM) can be attributed to two distinctive mechanisms. First, photoionization of the surrounding neutral gas by the strong, energetic ultraviolet (UV) flux of nearby massive stars is largely responsible for the detection of the standard hydrogen Balmer series, typically used for the morphological and kinematical description of H II regions. Secondly, stellar winds with high terminal velocities and violent supernova blasts are commonly associated with the propagation of transonic and supersonic shock waves in the surrounding medium. The important increase of the post-shocked gas' temperature favours its ionization through shock excitation.

Pioneering work by Sabbadin, Minello & Bianchini (1977) has compared specific flux ratios for a variety of ionic transitions in the ISM optical gas. This allowed the authors to approximately separate standard H II regions and planetary nebulae (PNe) mostly

governed by photoionization from shock-dominated supernova remnants (SNRs). These diagnostic diagrams were often used, in the literature, to classify large amount of ionized targets in large-scale objects, for example more-or-less distant galaxies (e.g. Magrini et al. 2003; Riesgo & López 2006). This has led to emission-line ratio plots in which each object is usually statistically represented by a single point. Obviously, intrinsic variations, within a given object, can be investigated by targeting Galactic objects individually (e.g. Phillips & Cuesta 1998, 1999; Phillips, Cuesta & Ramos-Larios 2010). This allows us to spatially resolve much smaller ( $\ll 0.1$  pc) structures and artefacts characterized by peculiar line ratios that are, otherwise, unrevealed or statistically negligible in observations using poorer angular resolutions. The investigation of close ionized objects has already revealed that photoionization and shock excitation can both be found in individual regions.

Kinematically speaking, standard H II regions encompassing massive stars earlier than O6 have shown little indication of a strong impact on the surrounding gas attributed to stellar winds, referred to earlier as a potential source for shock excitation in nebulae. This remains usually true even when using observations with high

★E-mail: dominic.lagrois.1@ulaval.ca

spectral resolutions that allow us to measure velocity fluctuations down to a few  $\text{km s}^{-1}$ . The main reason for this resides in the double-shock model said to accurately describe the dynamical evolution of wind-blown bubbles (Weaver et al. 1977). The reverse shock quickly (i.e. often within less than a spatial element of resolution) converts high-velocity ( $>1000 \text{ km s}^{-1}$ ) terminal winds into low-velocity, high-temperature gas. The thermal energy of this hot, pressurized material then initiates and fuels the expansion of the dense shell of post-shock ISM material found at much greater distances with respect to the central star. The typical expansion velocity of the shocked shell is usually a few  $\text{km s}^{-1}$  above  $10 \text{ km s}^{-1}$ , roughly the speed of sound for warm ( $\sim 10\,000 \text{ K}$ )  $\text{H}^+$  gas. Unfortunately, in complex tridimensional geometries, this kind of velocities could be easily confused with standard accelerated outflows in  $\text{H II}$  regions, such as Champagne (Bodenheimer, Tenorio-Tagle & Yorke 1979; Tenorio-Tagle 1979) or photoevaporated (Arthur & Hoare 2006; Mellema et al. 2006) flows, turbulent motions (Joncas & Roy 1984; Arsenault & Roy 1988; Lacrois & Joncas 2011) or fluid instabilities. This work mainly explores the possibility of detecting shock waves associated, in particular, with stellar winds using the emissive properties of the ionized gas rather than a more typical, and not always successful, approach based on the information retrieved from radial velocities and non-thermal line widths.

The IC 1805 nebula is located in the Perseus arm of our Galaxy. The most massive stars of the Melotte 15 star cluster are currently responsible for the energetic support of the large  $\text{H II}$  region. The south-central portion of the nebula (see Fig. 1), in the direct vicinity of the star cluster, is gas-rich and will be used in this work to fill the Sabbadin et al. (1977) diagrams. Our goals are to (1) obtain reliable,

high signal-to-noise ratio (S/N), spectra of the optical emission in the brightest portions of the IC 1805 star-forming complex; (2) provide the corresponding series of line-ratio diagnostic diagrams; and (3) investigate the impact of photoionization and shock excitation in the targeted gas volume.

We present, in Section 2, the Galactic  $\text{H II}$  region IC 1805 and its associated star cluster, Melotte 15. Information related to our spectrometric observations and methods used for data reduction are detailed in Section 3. Results of our study and diagnostic diagrams are provided in Section 4. Interpretation and discussion follow in Section 5. Summarized results and general conclusions will finally be provided in Section 6.

## 2 THE IC 1805 GAS COMPLEX

Introduced by Westerhout (1958) as an irregular nebula of medium brightness, the Galactic  $\text{H II}$  region IC 1805 is often referred to as the Heart nebula due to the heart-shaped morphology of its Southern hemisphere ( $60^\circ 28' \leq \delta_{2000} \leq 62^\circ 10'$ ). It is suggested that outflows from the OB association Melotte 15 ( $\alpha_{2000} = 02^{\text{h}}32^{\text{m}}45^{\text{s}}$ ,  $\delta_{2000} = 61^\circ 26' 40''$ ) are responsible for the actual expansion of the large  $\text{H II}$  region/superbubble (Basu, Johnstone & Martin 1999). Proper motion investigation has allowed the identification of 126 stars intrinsic to the star cluster (Shi & Hu 1999). The authors confirmed, through spectroscopic observations, the presence of numerous massive stars; about 40 from spectral types O4 to B2 (including 10 O-type stars) have been identified with a high probability of membership. An important proportion of these massive stars are still found on the main-sequence branch indicating a very young

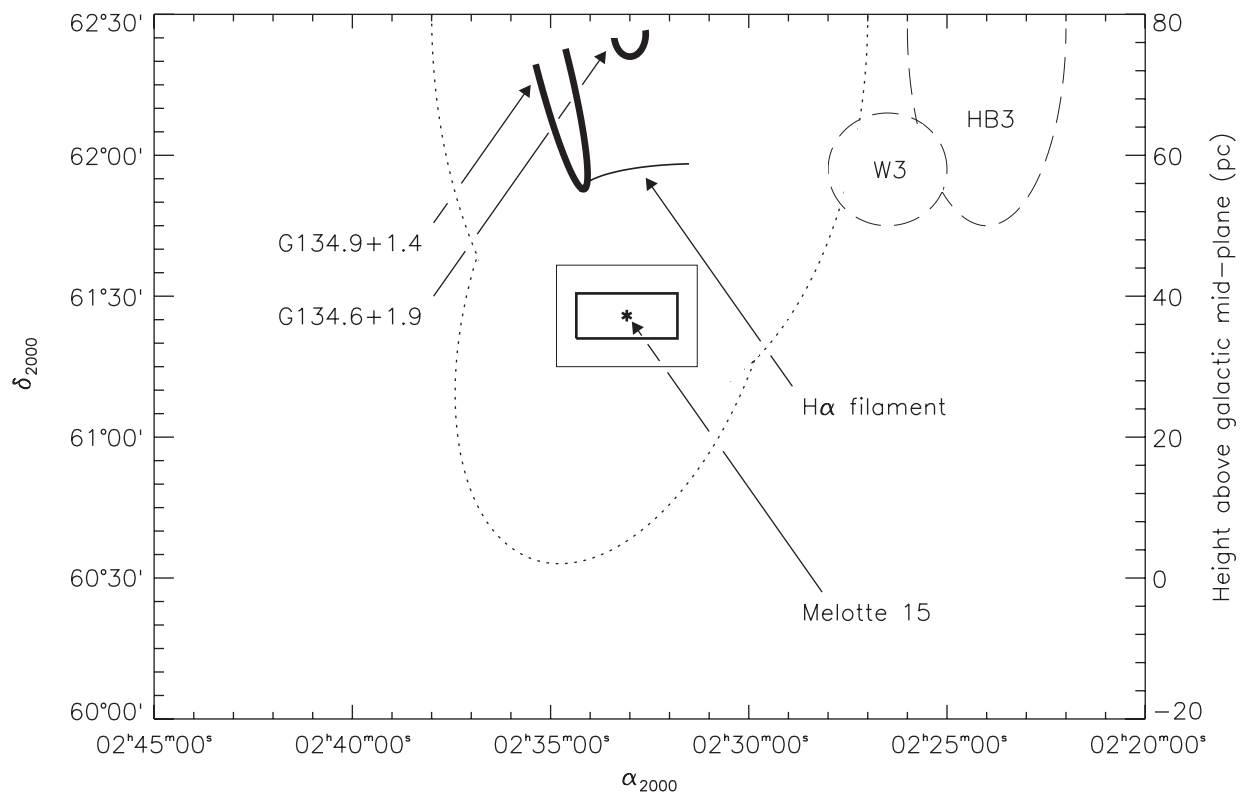


**Figure 1.** Schematic diagram of the southern portions of the IC 1805 nebula (circumscribed by the dotted line). The regular and thick lines trace out the  $\text{H}^+$  and CO (2–1) structures, respectively (see fig. 1 of Lacrois & Joncas 2009a). The thin-line box approximately delineates the gas-rich region in the vicinity of the Melotte 15 star cluster. The thick-line box approximately indicates the extended FOV of our spectrometric observations. Also included in the diagram are the nearby  $\text{H II}$  region W3 and the supernova remnant HB3 (long-dashed lines).

cluster age evaluated at 2.5 Myr (Llorente de Andrés, Burki & Ruiz del Arbol 1982). The dynamical age of the IC 1805 nebula being estimated at 14 Myr (Lagrois & Joncas 2009b), it appears that the large H II region was formed and shaped by the mechanical deposit, in the ISM, of energy (i.e. photon flux, stellar winds and supernovae) attributed to a succession of different star clusters, Melotte 15 being the most recently formed. No non-thermal emission being actually detected in the large star-forming complex, this suggests that the impact of old supernovae could be negligible in the nebula's current dynamics. *UBV* photometry, properly corrected for absorption, puts the Melotte 15 complex at a heliocentric distance of 2.35 kpc (Massey, Johnson & DeGioia-Eastwood 1995).

Lagrois & Joncas (2009a,b) provide a high spectral-resolution ( $< 15 \text{ km s}^{-1}$ ) kinematical investigation of the H<sup>+</sup> content on an appreciable fraction of the IC 1805 ionized extent. The northernmost portions ( $63^{\circ}20' \leq \delta_{2000} \leq 66^{\circ}50'$ ) of the large ovoid bubble have shown kinematical evidence for high-latitude gas venting and the early development of a Galactic chimney. It appears that leaking UV photons, emanating from the Melotte 15 star cluster and unabsorbed by the denser low-declination material, may participate in the sustainment of the high-temperature gas found in the Galactic halo. In the southern half of the nebula, schematically represented in Fig. 1, the last residual fragments of an old giant molecular cloud appear to be eroded by the UV flux and stellar winds of the nearby massive stars. As a result, a series of criss-crossing accelerated flows are detected in agreement with the Champagne phase (e.g. Bodenheimer et al. 1979; Tenorio-Tagle 1979; Tenorio-Tagle & Bedjin 1981; Tenorio-Tagle et al. 1982).

Ionization fronts, stellar winds and Champagne shocks are therefore expected to have developed in the vicinity of the Melotte 15 star cluster. This could suggest that shock excitation may be responsible for the presence of a certain fraction of the observed ionized material although a well-defined kinematical signature attributed to shock waves has not been formally identified in our previous study. This will be largely addressed in the following sections.

### 3 OBSERVATIONS AND DATA REDUCTION

Observations of the IC 1805 optical gas complex were performed during the nights of 2008 September 24–25 and 25–26 using the Ritchey-Chrétien 1.6-m telescope of the Observatoire du Mont-Mégantic (OMM). The data were gathered using the imaging Fourier transform spectrometer SpIOMM (Spectromètre Imageur de l'Observatoire du Mont-Mégantic). Technical details regarding SpIOMM are provided in Bernier et al. (2008), Drissen et al. (2008) and references therein.

For each pixel of the detector, the instrument has the capacity to obtain the emission spectrum of the corresponding nebular-gas column in selected bandwidths of the optical regime between 3500 and 9000 Å. Prior to entering the observation mode, the spectral resolution is fixed by the observer between  $R = 1$  and 25 000.

For this work, the use of an interference filter enabled the acquisition of the spectral information in the red portion of the electromagnetic spectrum between 6480 and 6820 Å. This allowed us to obtain, simultaneously, emission spectra displaying the H $\alpha$   $\lambda$ 6563 Å, [N II]  $\lambda$ 6548, 6584 Å, and [S II]  $\lambda$ 6716, 6731 Å ionic transitions. A spectral resolution of  $R = 2100$  was judged appropriate corresponding to a resolution of roughly 3 Å or  $150 \text{ km s}^{-1}$  centred on the H $\alpha$  rest frequency. The field of view (FOV) is roughly  $12 \times 12 \text{ arcmin}^2$  while data were spatially binned  $2 \times 2$  during acquisition to reduce readout times.

**Table 1.** Observational parameters at data acquisition.

Observational parameters		Field	
		East	West
Optical centre	$\alpha_{2000}$	02 <sup>h</sup> 33 <sup>m</sup> 55 <sup>s</sup>	02 <sup>h</sup> 32 <sup>m</sup> 35 <sup>s</sup>
	$\delta_{2000}$	61°27'30''	61°27'30''
Seeing at acquisition	(arcsec)	2.5	2.8
Spatial resolution	(arcsec pixel <sup>-1</sup> )	2.2	2.2
	(pc pixel <sup>-1</sup> )	0.026	0.026
Spectral range	(Å)	6480–6820	6480–6820
Spectral resolution	(km s <sup>-1</sup> )	3	3
	(s)	150	150
Exposition time per channel	(s)	32	35
Number of channels		249	249

The resulting raw data cube is formed, for each pixel, of a discrete interferogram. Following classical data reduction for CCD observations (i.e. bias subtraction and flat-field correction), all panchromatic images were realigned to correct for guiding errors. According to the photometry of stars located in gas-depleted zones, all images were also corrected for variations of the sky transparency occurring during data acquisition. Each interferogram is then Fourier transformed and calibrated in velocities using a He–Ne laser ( $\lambda$ 6328 Å) as frequency of reference. The data were again spatially binned  $2 \times 2$  during reduction in order to account for the 2.5 arcsec seeing measured at the telescope. The resulting spatial resolution is of 2.2 arcsec pixel<sup>-1</sup> for  $325 \times 335 \text{ pixel}^2$ . Using the adopted distance to Melotte 15 (see Section 2), this corresponds to an angular resolution of 0.026 pc pixel<sup>-1</sup> as seen on the plane of the sky.

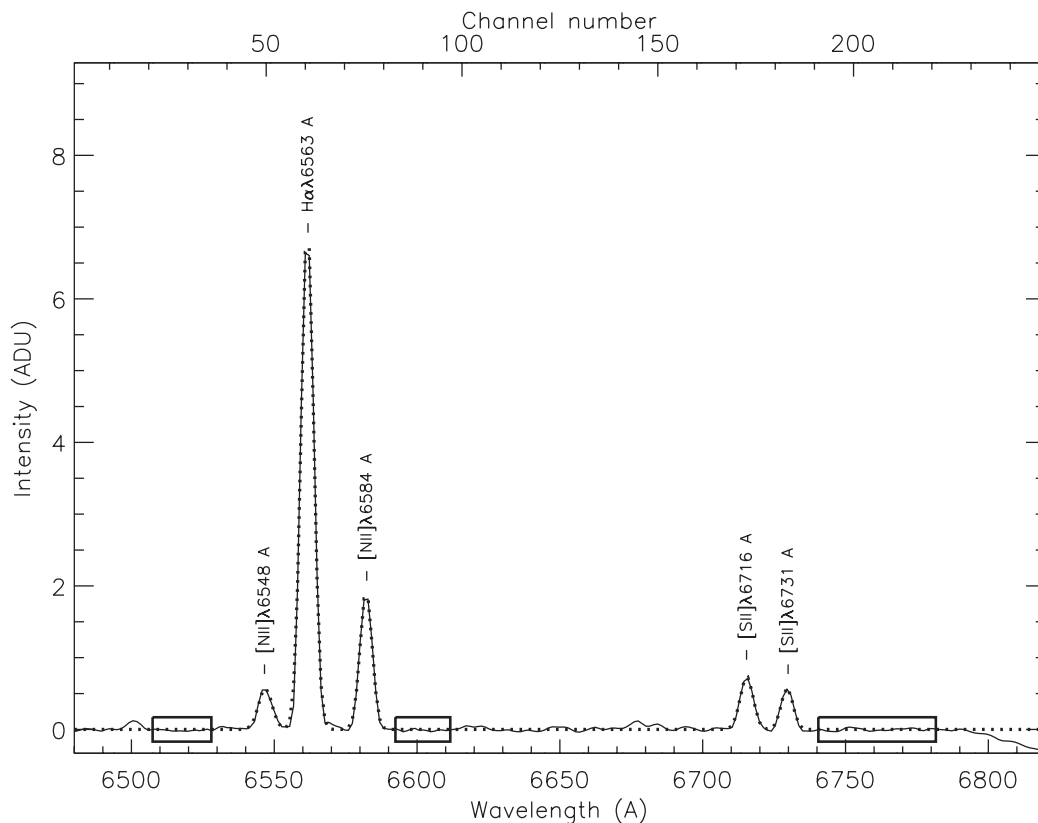
Two cubes were obtained in the vicinity of the Melotte 15 star cluster. The observational parameters for both cubes, labelled east and west, are summarized in Table 1. The heliocentric correction being very similar for both cubes, the two were mosaicked to a new extended FOV of  $21.5 \times 12.5 \text{ arcmin}^2$  (see Fig. 1) and over 200 000 emission spectra. Following subtraction of the continuum, a multi-component Gaussian fit procedure written in IDL was applied to the mosaicked cube. The fitting procedure returns, for each component, the peak intensity in Analog-to-Digital Units (ADU), the line centroid (or velocity) and the line dispersion ( $\sigma \equiv \text{FWHM}/2.354$ ). Since this work is mostly based on line ratios, we followed the recommendation of Rola & Pelat (1994) by imposing an S/N greater than 6 for a given Gaussian fit to be usable. For each spectrum, the noise level was estimated from continuum fluctuations measured in empty channels.

Fig. 2 shows a high-quality spectrum obtained in the brightest parts of our mosaicked cube. This kind of spectrum is typical only for the regions of high emissivity of our FOV. Emission-line profiles corresponding to weaker areas are much noisier and complementary lines, found in the wavelength interval covered by the interference filter (see above), such as the [N I]  $\lambda$ 6500 Å and [He I]  $\lambda$ 6678 Å transitions are not discernible from noise fluctuations. The weakest line (i.e. [N II]  $\lambda$ 6548 Å) in the example provided by Fig. 2 has an S/N of 24.

## 4 RESULTS

### 4.1 Monochromatic maps

Figs 3–7 provide the monochromatic, peak-intensity maps for all five emission lines investigated in this work. North is up and east is to the left in all figures. Fig. 8 spectacularly displays the [N II]  $\lambda$ 6584/H $\alpha$   $\lambda$ 6563 ratio throughout the whole FOV (see the caption). Red emphasizes regions dominated by H $\alpha$  while bluer



**Figure 2.** High-quality emission spectrum recovered from our spectrometric observations of the brightest parts of the IC 1805 gas complex. The raw data are displayed as the regular line. Gaussian fits are represented as the dotted line. The boxes indicate the inter-line channels where the noise level was estimated. All five ionic transitions, targeted in this work, are listed. The S/N varies from 24 to 298 from [N II]  $\lambda$ 6548 Å to H $\alpha$   $\lambda$ 6563 Å.

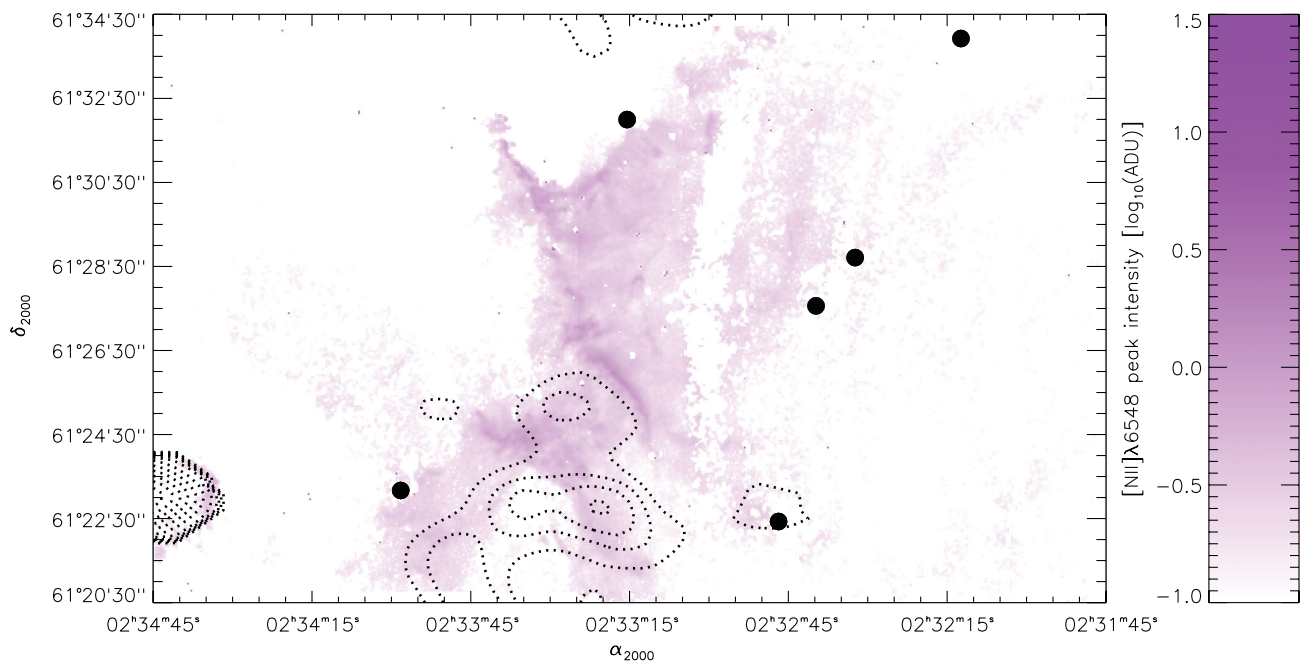


**Figure 3.** Peak-intensity map of the [N II]  $\lambda$ 6548 Å ionic transition in IC 1805. Only emission-line profiles with S/N > 6 were considered. A log<sub>10</sub>-scale filter was applied in order to emphasize fainter ionized structures. As listed by Massey et al. (1995), the filled circles indicate the position of the six O-stars found in the FOV. Dotted contours are traced out using an integrated intensity map of the molecular emission obtained from the FCRAO CO (1–0) observations. The spectral collapse of the molecular data cube was made for local standard of rest (LSR) radial velocities between  $-22.90$  and  $-63.30$  km s<sup>−1</sup>, approximately corresponding to the extrema in velocities measured in the H<sup>+</sup> gas closest to Melotte 15 (Lagrois & Joncas 2009a). 11 contour levels are drawn between 2 and 12 K km s<sup>−1</sup>. The FCRAO CO (1–0) subcube has a noise level slightly below 1 K.



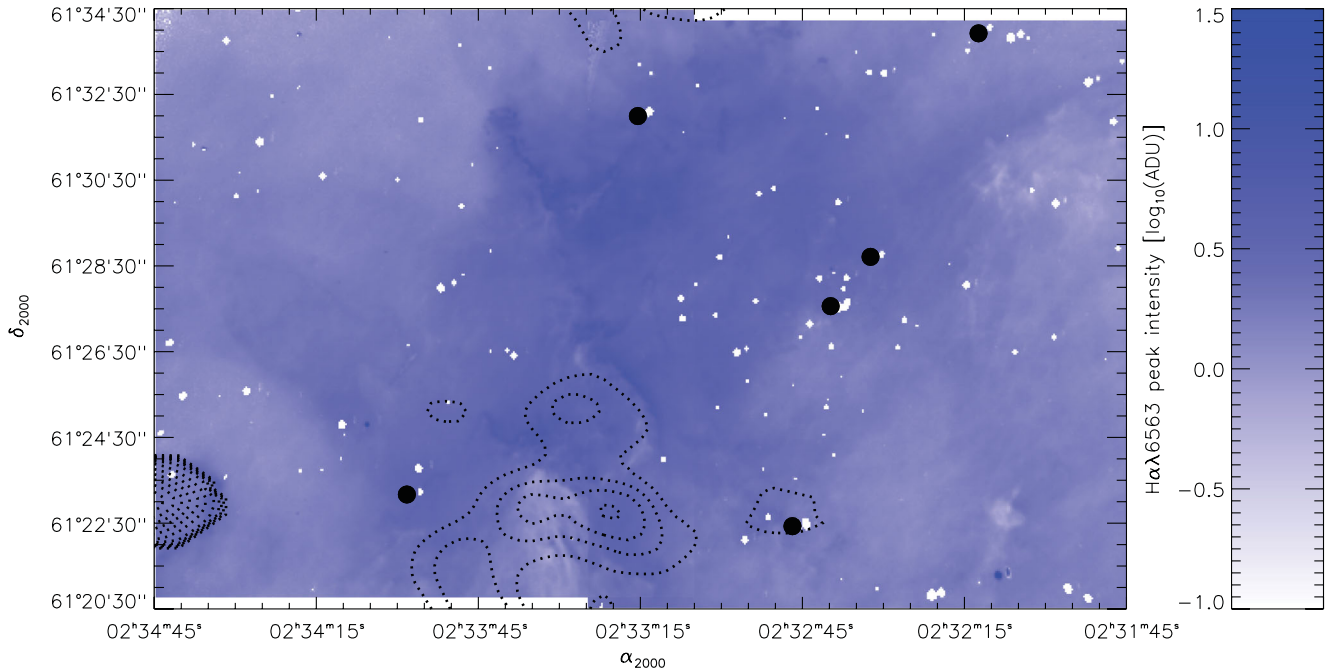


**Figure 4.** Peak-intensity map of the  $H\alpha$   $\lambda 6563$  Å ionic transition in IC 1805. More details are provided in the caption of Fig. 3.

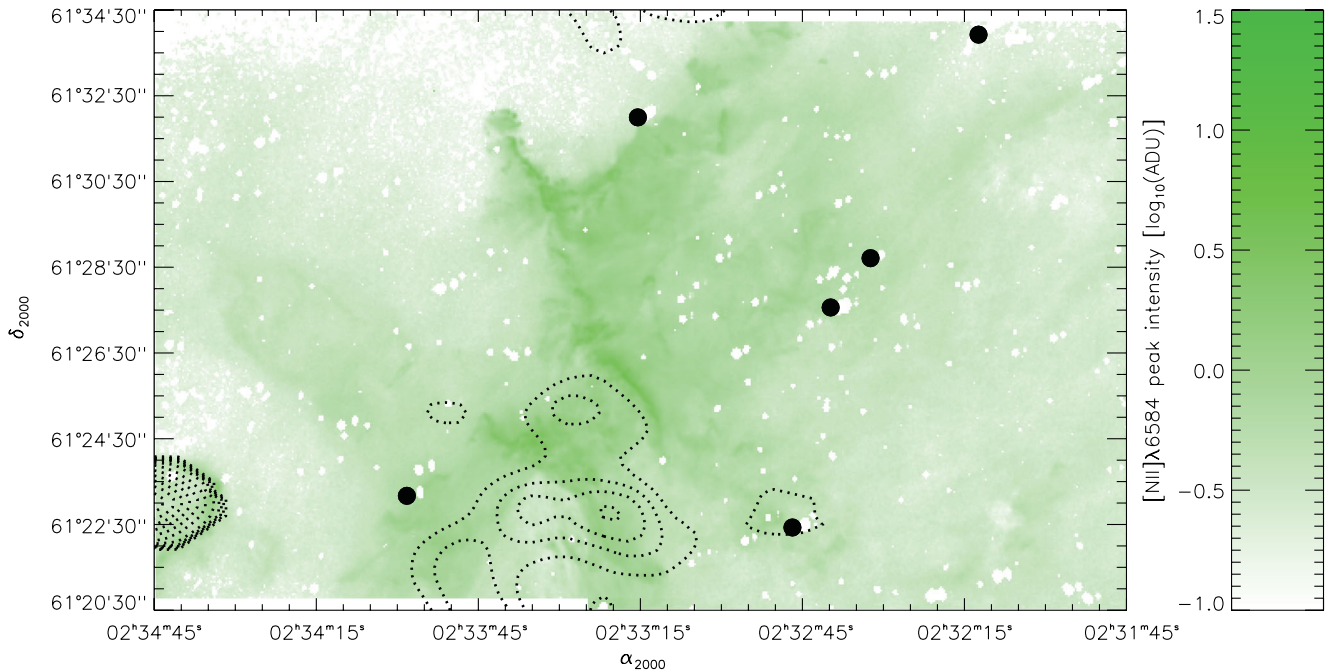


**Figure 5.** Peak-intensity map of the  $[N II]$   $\lambda 6584$  Å ionic transition in IC 1805. More details are provided in the caption of Fig. 3.

shades pinpoint a stronger emission of the  $[N II]$   $\lambda 6584$  Å transition (with respect to the redder areas). Three stars with strong  $H\alpha$  lines are detected (the third being barely perceptible very close to the centre of the figure). At the position of all other stars, bad pixels were removed and replaced by mean values statistically representing the surrounding nebular-gas content. This figure is particularly useful in describing ionized features in our FOV.

The Five College Radio Astronomy Observatory (FCRAO) CO(1–0) survey of the second Galactic quadrant (Heyer et al. 1998)

has revealed very faint emission corresponding to tenuous molecular material at the position of the bright, central ionized structure in Figs 3–7. This suggests the presence of a large molecular fragment, surrounded by the most massive stars of the Melotte 15 cluster, which has undergone almost full erosion by the UV flux and stellar winds of the nearby ionizing sources. Fig. 8 reveals the filamentary nature of the central structure. These filaments most likely trace out the spatial disposition, on the plane of the sky, of the eroded (sometimes fully ionized) molecular envelopes. The central structure is surrounded by diffuse ionized material likely associated with

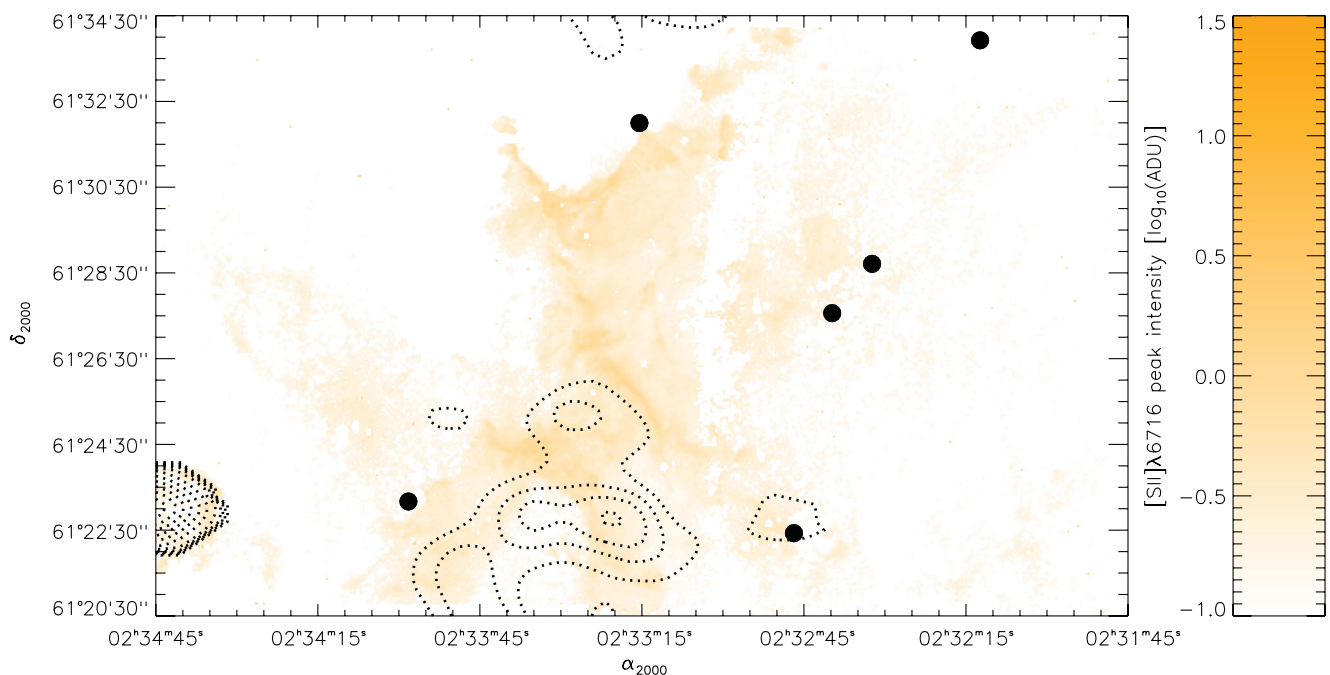


**Figure 6.** Peak-intensity map of the [S II]  $\lambda 6716$  Å ionic transition in IC 1805. More details are provided in the caption of Fig. 3.

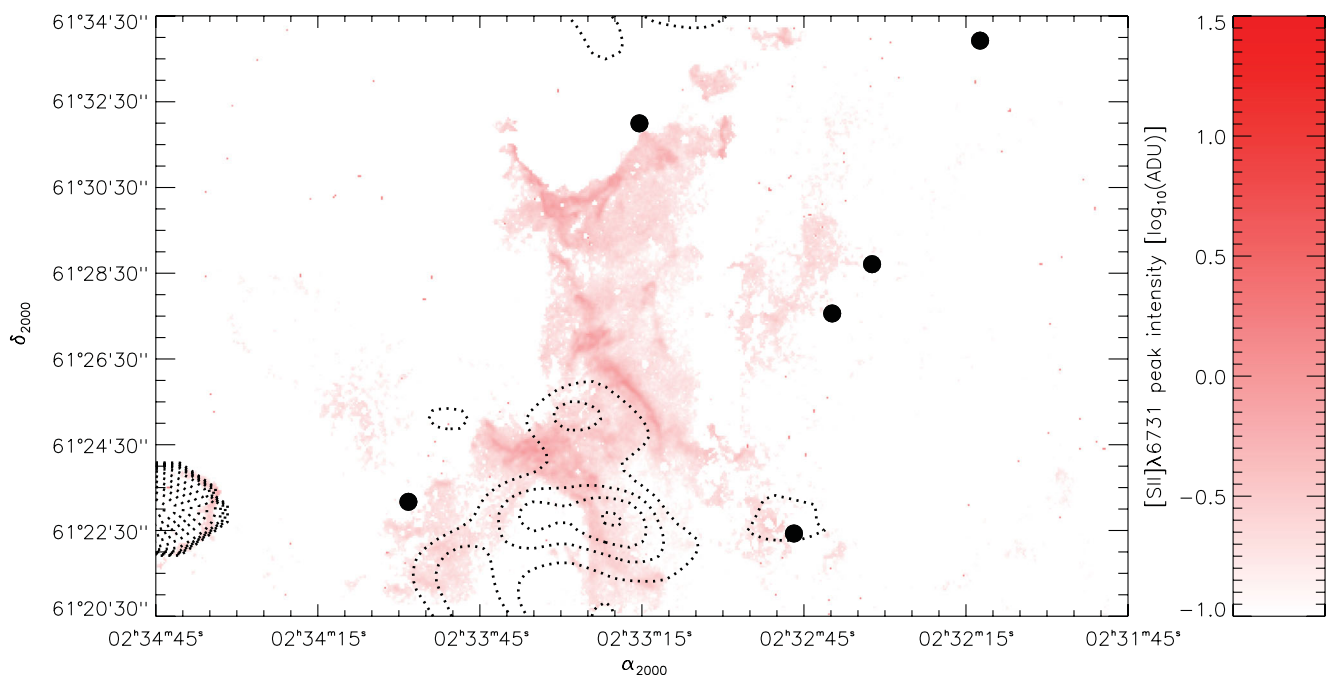


**Figure 7.** Peak-intensity map of the [S II]  $\lambda 6731$  Å ionic transition in IC 1805. More details are provided in the caption of Fig. 3.

photoevaporated flows kinematically in agreement with the Champagne phase (Lagrois & Joncas 2009a). One of these flows (displaying blue shades in Fig. 8) is particularly well defined, propagating from the bottom centre of our FOV approximately towards the upper-left corner of Fig. 8. West of the central structure, the spatial arrangement of the nebular gases is extremely complex. Ionized filaments are still perceptible although the contrast with the diffuse surroundings is not as clear. Towards the western boundary of Fig. 8, even the  $H\alpha$  emission appears darker, obscured by interstellar dust. Shock excitation in the vicinity of the bright, central

ionized structure, displayed in Figs 3–8, will be largely discussed and investigated in Section 5.2.1.

Towards the south-eastern portion of our FOV, a small CO fragment is clearly detected in the FCRAO survey at the systemic velocity of the IC 1805 region (see CO contours in Figs 3–7). Its ionized counterpart is revealed by a thin, rounded ionization front especially visible in the lower-left corner of Fig. 8 (see also Fig. 19a). This specific shape of the ionization front results from the vast majority of the ionizing sources in Melotte 15 being located behind the molecular clump. This was kinematically



**Figure 8.** Image of the  $[\text{N II}] \lambda 6584 / \text{H}\alpha \lambda 6563$  ratio in central IC 1805. Red shades indicate that the  $\text{H}\alpha$  component clearly dominates the signal. Blue shades show the position of particularly bright  $[\text{N II}] \lambda 6584 \text{ \AA}$  emission. Stars were removed if not for three of them having well-defined, strong  $\text{H}\alpha$  emission (see the text). This image was not processed using the information retrieved from the Gaussian fits but rather by simply collapsing the initial mosaicked cube in the channel intervals respectively enclosing the  $\text{H}\alpha \lambda 6563 \text{ \AA}$  and  $[\text{N II}] \lambda 6584 \text{ \AA}$  ionic lines (e.g. see Fig. 2).

confirmed, in Lagrois & Joncas (2009a), by the detection of an accelerated ionized outflow moving away from the observer (see Section 5.2.2.1). This flow eventually collides or simply coincides in lines of sight with the south-central/north-east flow mentioned in the previous paragraph. This results in particularly complicated kinematical motions in central IC 1805 with  $\text{H}\alpha$  non-thermal line widths approaching the supersonic regime ( $\sim 10 \text{ km s}^{-1}$ ) according to high-resolution observations (Lagrois & Joncas 2009a).

In the same area of Fig. 8 (see also Fig. 19c), a cylindrical, cigar-like feature appears to be associated with an isolated star with strong  $\text{H}\alpha$  lines (see above). The feature has bright  $\text{H}^+$  and  $\text{N}^+$  rims but is almost completely gas-deprived near its centre. This structure as well as the rounded ionization front found in the lower-left corner of Fig. 8 will be discussed in Section 5.2.2.

Fig. 9 was processed identically to Fig. 8 and displays the  $([\text{S II}] \lambda\lambda 6716, 6731) / [\text{N II}] \lambda 6584$  ratio (where the numerator is the sum of both lines of the  $[\text{S II}]$  doublet). Again, blue shades

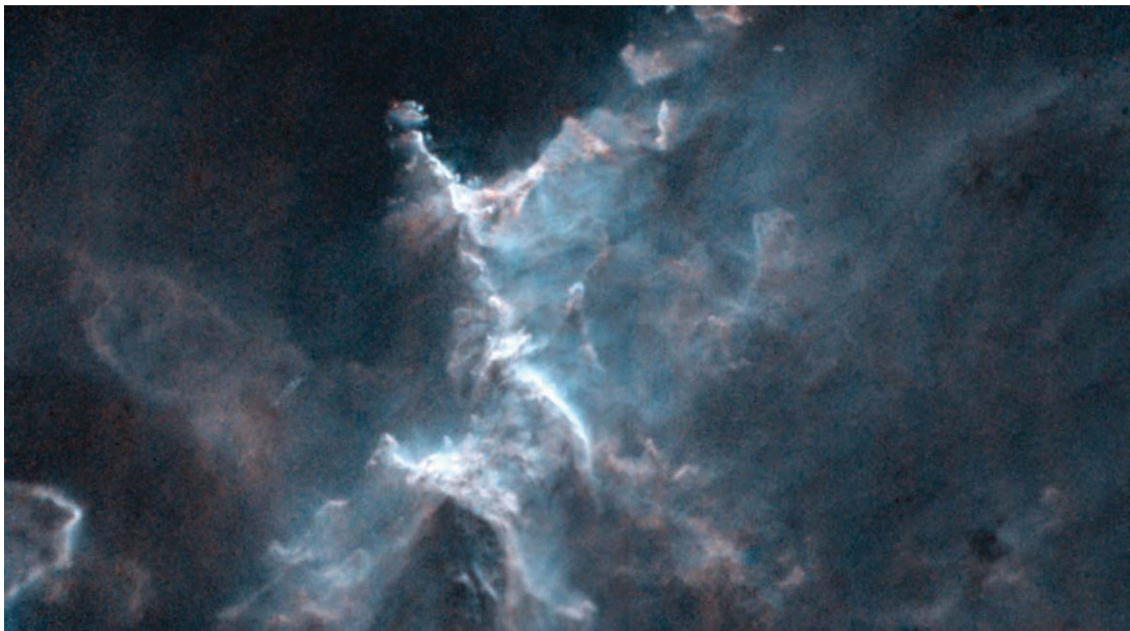


**Figure 9.** Image of the  $([\text{S II}] \lambda\lambda 6716, 6731) / [\text{N II}] \lambda 6584$  ratio in central IC 1805. Blue shades indicate that the  $[\text{N II}]$  component clearly dominates the signal. Red shades show the position of particularly bright  $[\text{S II}]$  emission. The image was processed identically to Fig. 8.



identify nitrogen-rich zones while red areas indicate that a sizeable role is played by sulphur in the overall gas emissivity. One immediately notices the complexity of the chemical properties in IC 1805. While [N II] clearly dominates over [S II] where H $\alpha$  is the brightest, weaker zones (in H $\alpha$ -integrated intensity) show an important increase of the relative contribution of the sulphur material. In particular, the reader's attention is directed towards the north-eastern filament of the bright, central structure described above. A series of small, quasi-circular blobs are found. The top three reveal two nitrogen-dominated features (in blue) and one with a stronger relative contribution in [S II] (in red). Investigating their corresponding spectrum, the [S II] intensity remains roughly constant from one blob to another, while the [N II] lines suffer a strong attenuation along the line of sight of the 'redder' one (which explains the relatively poor contribution of nitrogen towards it). This behaviour is not generalized to our whole FOV although similar features can be found here and there.

The supernova remnant HB3 (see Fig. 1) is located too far away from our FOV to have had a sizeable impact on the chemical properties in central IC 1805. Alternatively, we can argue that the old, large molecular cloud, which gave birth to Melotte 15 roughly 2.5 Myr ago, may have had an inhomogeneous distribution of its chemical compounds. Old supernovae in IC 1805, whose non-thermal emission has vanished since, could also be held responsible. We reiterate that the IC 1805 region was most likely formed by a succession of different star clusters (see Section 2), i.e. although no indication for supernova remnants is currently found inside the large H II region, it is highly probable that the inner zones of IC 1805 were, at some time in the past, disturbed by supernova events associated with previous generations of massive stars. These stars could have had an intrinsic inhomogeneity in their inner nitrogen distribution which eventually led to an anisotropic dispersion of these chemical compounds, products of the CNO cycle, as each stellar object reached the end of its life (e.g. see the works by MacAlpine et al. 2007, MacAlpine & Satterfield 2008 and Charlebois et al. 2010 on the Crab nebula).

## 4.2 Diagnostic line ratios

### 4.2.1 Definition

Line ratios, in the literature, usually correspond to ratios between two (or more) line fluxes. For a given emission line, the line flux is proportional to the product between its peak intensity and its width as returned by the Gaussian fit. In this work, the relatively low spectral resolution used (see Section 3) is roughly a factor 10–20 greater than typical non-thermal velocity fluctuations, along the line of sight, found in IC 1805 using high-resolution observations of the H $^+$  kinematics (Lagrois & Joncas 2009a). Hence, in this work, the width of each emission line is entirely dominated by the instrumental response and the returned widths are very similar, from one ion to another, independent of the position in the FOV. Therefore, line ratios in the following discussion were strictly estimated using returned values for peak intensities while line widths were simply not considered.

### 4.2.2 Line profile selection

To ensure the selection of the most reliable emission-line profiles in our sample of over 200 000 spectra, a series of conditions are proposed. All of them need to be fulfilled, otherwise the given

spectrum is rejected from the discussion to follow. The conditions are summarized as follows.

(i) The profile must show all five lines (i.e. H $\alpha$   $\lambda$ 6563 Å, [N II]  $\lambda$ 6548, 6584 Å, and [S II]  $\lambda$ 6716, 6731 Å) investigated in this work with a reliable S/N of above 6.

Two conditions are proposed in order to confirm that the kinematical properties of a given profile are physically acceptable.<sup>1</sup> More specifically, the [N II]  $\lambda$ 6548 Å and [N II]  $\lambda$ 6584 Å transitions must exhibit identical non-thermal motions since both lines are emitted by the same ions. The same argument also applies to the [S II]  $\lambda$ 6716 Å and [S II]  $\lambda$ 6731 Å lines.

(ii) First, the difference, in centroid velocities, between both lines of a given doublet (i.e. [N II] or [S II]) must not exceed 15 km s $^{-1}$ . This corresponds roughly to 1/10th the spectral resolution of our observations (see Section 3) and therefore roughly accounts for the uncertainties on the Gaussian fits. Centroid-velocity differences, along a given line of sight, between the H $^+$ , N $^+$  and S $^+$  material are allowed (and expected) since all three ions are not necessarily co-spatial in central IC 1805.

(iii) Secondly, the difference, in measured line widths, between all five components must not exceed 15 km s $^{-1}$ . This is expected from all lines being dominated by the instrumental response (see Section 4.2.1). If observations with high spectral resolution (e.g. of the order of a few km s $^{-1}$ ) were used here, a condition similar to the previous one (on centroid velocities) would have been required (i.e. identical line widths, within the uncertainty bars of the Gaussian fits, between both lines of a given doublet, [N II] or [S II]).

Finally, specific line ratios of the [N II] and [S II] transitions must agree with standard theoretical models of ionized nebulae.

(iv) The computation of the [S II]  $\lambda$ 6716/[S II]  $\lambda$ 6731 line ratio must lead to a finite electron density. The upper and lower uncertainties on the density measurement (see Section 4.2.3) must also be finite.

(v) The computation of the [N II]  $\lambda$ 6584/[N II]  $\lambda$ 6548 line ratio must not largely deviate from the theoretical value approaching 3 in low-density regimes typically found for H II regions. Small deviations from 3 are expected (see Section 4.2.4) and explained (see Section 5.1) although values of  $\ll 2$  or  $\gg 4$  would seem particularly hard to reconcile with the theory and would therefore demand to be rejected.

All conditions taken in consideration, only 3057 emission-line profiles were retained, most of them being associated with the bright, central structure found in the overlapping region between the eastern and western fields (see Section 5.2.1). Obviously, the summation of both cubes largely contributes to increase the data quality for duplicated pixels not only by increasing the peak signal for all lines but also by flattening noise fluctuations in empty channels (see Fig. 2).

Considering the very large number of emission-line profiles available in our initial data set (more than 200 000), we are fully aware that the conditions listed above drastically reduce the size of the retained sample. On the other hand, these conditions ensure that the retained profiles are undoubtedly the most reliable available.

<sup>1</sup> Although this paper is based on line-ratio measurements, kinematical properties were also carefully investigated. The question arises: could the line fluxes of kinematically 'unacceptable' emission-line profiles [i.e. that do not fulfil conditions (ii) and/or (iii)] be trusted? At this point, we have no reliable method to further investigate the question. We therefore chose to avoid any possible controversy/confusion on the matter and simply reject those kinematically peculiar spectra.



We reiterate that an S/N greater than 6 is required to appropriately conduct an investigation on line ratios. However, a ‘physical detection’ (of a given line) is considered when  $S/N \gtrsim 3$  (Rola & Pelat 1994). This will be used in a later subsection to investigate notable, although not necessarily reliable, line ratios for particular structures in IC 1805 (see Section 5.2.2.2).

#### 4.2.3 Electron densities computed from the [S II] doublet

The [S II]  $\lambda 6716$ /[S II]  $\lambda 6731$  line ratios were computed and used as input values for the Fivel FORTRAN procedure (De Robertis, Dufour & Hunt 1987) adapted, for convenience, in IDL. Assuming a constant electron temperature of 7400 K throughout IC 1805 (Lagrois & Joncas 2009a), mean electron densities ( $\rho$ ) in the S<sup>+</sup> ionic volume were obtained for each nebular-gas column (i.e. line of sight).

Since uncertainties cannot be recovered from the use of the Fivel procedure, error bars on density measurements  $\rho$  were computed as follows. For each line of the [S II] doublet, the uncertainty on the peak intensity, as returned by the Gaussian fit procedure, is provided by equation (4a) of Landman, Roussel-Dupré & Tanigawa (1982). From there, the statistical error on each line ratio is simply provided by the standard propagation of uncertainty. For each ratio, minimal and maximal plausible values are then easily obtained by

respectively subtracting and adding this calculated uncertainty. Using these lower and upper limits on [S II]  $\lambda 6716$ /[S II]  $\lambda 6731$ , maximal ( $\rho_{\max}$ ) and minimal ( $\rho_{\min}$ ) densities associated with  $\rho$  can be obtained via Fivel. An asymmetrical error bar usually results where the upper (lower) uncertainty is provided by the difference between  $\rho_{\max}(\rho)$  and  $\rho(\rho_{\min})$ . Only  $\rho$  values where both  $\rho_{\min}$  and  $\rho_{\max}$  are finite were retained (see Section 4.2.2). According to Fivel, this implies that  $\rho_{\min}$  and  $\rho_{\max}$  must be greater than  $10 \text{ cm}^{-3}$  and lower than  $15\,000 \text{ cm}^{-3}$ , respectively (these two values mostly depend on our choice of a constant electron temperature of 7400 K in IC 1805). Our method considers that the statistical error on  $\rho$  is entirely dominated by the data quality (i.e. S/N of the [S II] lines) and that the uncertainties on the atomic parameters used by Fivel are negligible. However, using  $\rho_{\max}$  and  $\rho_{\min}$  to calculate the statistical error on  $\rho$  probably overestimates the actual uncertainty on the electron density measurement.

The distribution of the retained electron densities is provided by the black curve in Fig. 10(a) (the blue and red distributions will be discussed in Section 5.2.1). The histogram has a mean of  $155^{+135}_{-75} \text{ cm}^{-3}$  where the error bars correspond to the mean upper ( $(\rho_{\max} - \rho)$ ) and lower ( $(\rho - \rho_{\min})$ ) uncertainty retrieved from the 3057 electron-density points preserved. Fig. 10(b) provides the spatial distribution of these points superimposed to a black-and-white reproduction of Fig. 4. Purple dots have the lowest density values while red dots have the largest (see the caption).

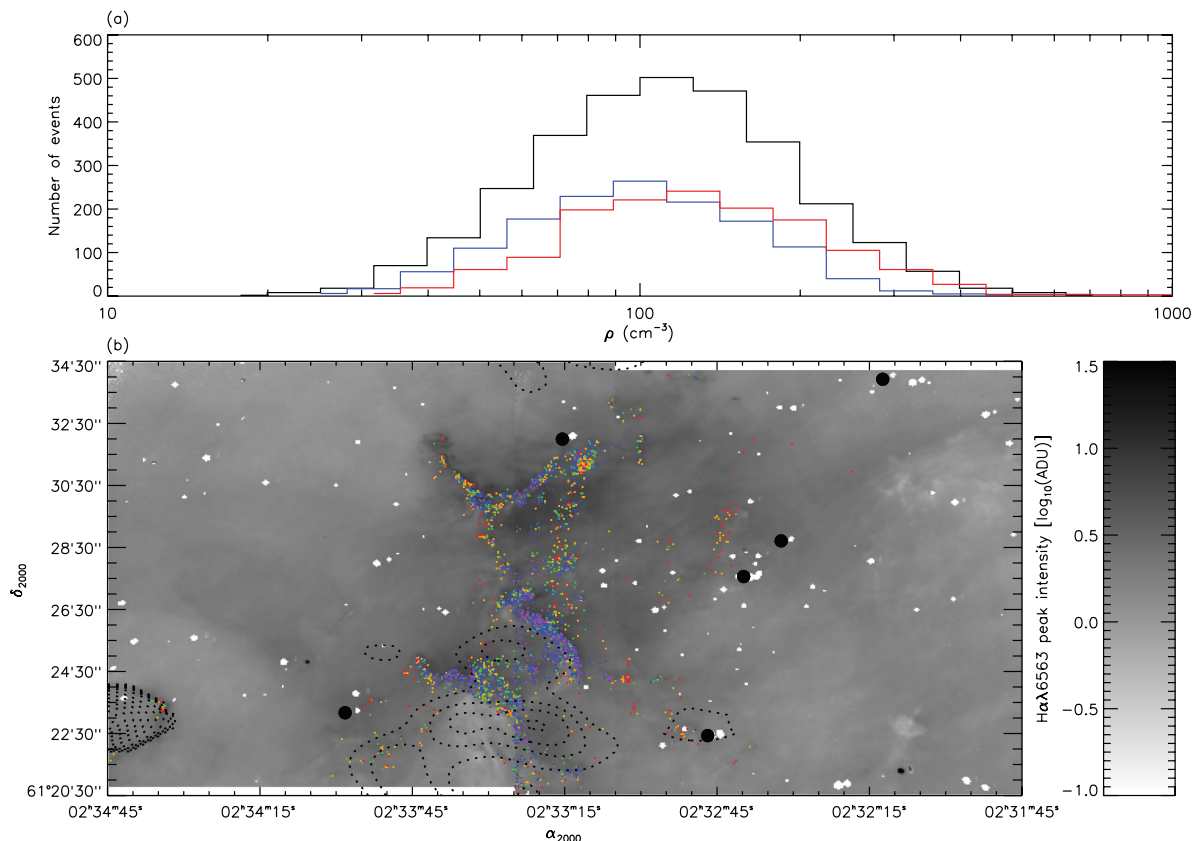


**Figure 10.** Panel (a): histograms of the mean electron densities ( $\rho$ ) in IC 1805 computed from the [S II]  $\lambda 6716$ /[S II]  $\lambda 6731$  line ratio. The black-line distribution corresponds to the 3057 emission-line profiles fulfilling all five conditions of Section 4.2.2. The blue curve is a subset of the black distribution, isolating the electron densities of specific points suggesting shock excitation. The red distribution uses the same points as the blue histogram although densities were computed from the post-subtraction [S II] doublets. The two coloured histograms are discussed in Section 5.2.1 (see the text). Panel (b): spatial distribution of all 3057 electron-density measurements forming the black histogram of panel (a). Densities between 1 and  $75 \text{ cm}^{-3}$  (purple dots), 75 and  $150 \text{ cm}^{-3}$  (blue dots), 150 and  $200 \text{ cm}^{-3}$  (green dots), 200 and  $300 \text{ cm}^{-3}$  (orange dots) and  $300+ \text{ cm}^{-3}$  (red dots) are displayed.

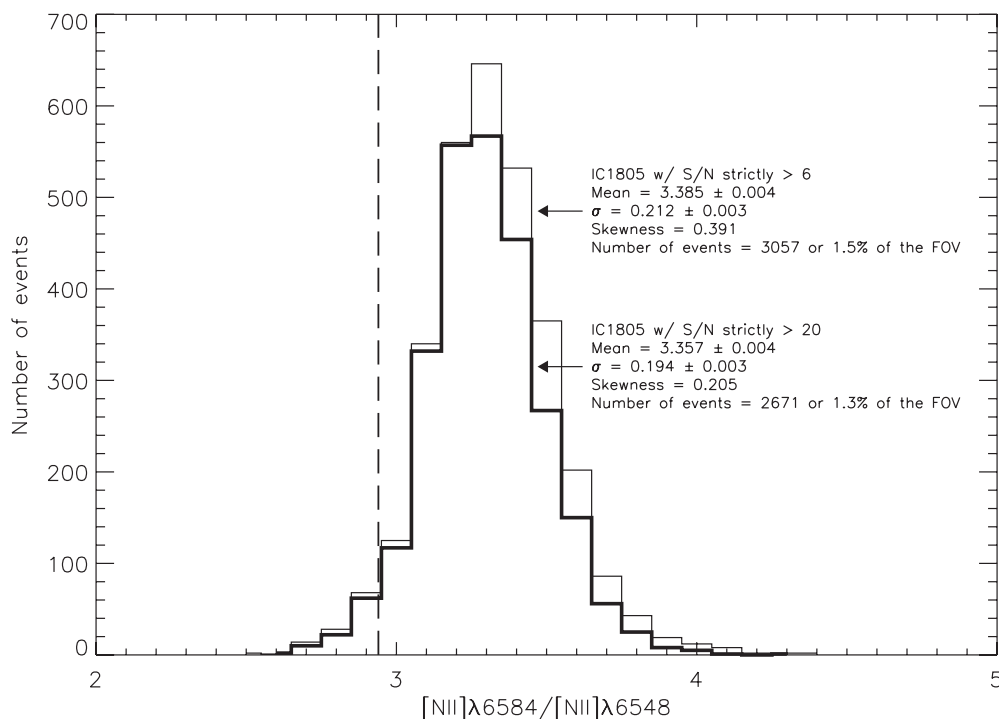


**Figure 11.** Histograms of the  $[\text{N II}] \lambda 6584/[\text{N II}] \lambda 6548$  line ratios in IC 1805. The theoretical value of 2.94, obtained in a low-density regime, is indicated by the long-dashed line. The regular-line distribution corresponds to the 3057 emission-line profiles fulfilling all five conditions of Section 4.2.2. The thick-line distribution considers only emission-line profiles with S/N greater than 20 (see the text). Statistical properties of both histograms are provided within the figure itself.

#### 4.2.4 The $[\text{N II}]$ line ratio

Fig. 11 provides the distribution of the  $[\text{N II}] \lambda 6584/[\text{N II}] \lambda 6548$  line ratio in the vicinity of the Melotte 15 star cluster. The vertical long-dashed line indicates the theoretical value as suggested by the ratio of the transition probabilities of both ionic lines in a low-density regime (Osterbrock & Ferland 2006, chapter 5). All 3057 points mentioned in Section 4.2.3 formed the regular line distribution. As shown by the thick-line histogram, the presence of large values, i.e. above  $\sim 3.5$ – $3.6$ , is reduced by considering only data points of very high quality (i.e. requiring here, arbitrarily, that  $\text{S/N} > 20$  in the first condition of Section 4.2.2). Uncertainties on the mean and one-standard deviation of both histograms are statistical uncertainties retrieved assuming normal distributions (Bevington 1969, chapter 5). Extreme values for  $[\text{N II}] \lambda 6584/[\text{N II}] \lambda 6548$ , i.e. below 2 or well above 4, were not measured. Hence, condition (v) listed in Section 4.2.2 was not used in this work to reject particular emission-line profiles, although it could be used by other authors for future, similar studies.

Considering the relatively high S/N used here (above 20 for the thick-line histogram of Fig. 11, hence suggesting a very good signal quality), deviations from  $([\text{N II}] \lambda 6584/[\text{N II}] \lambda 6548) \sim 3$  seem genuine and will be addressed in Section 5.1.

#### 4.2.5 Line-ratio diagnostic diagrams

Panels (a) in Figs 12–14 provide a series of line-ratio diagnostic diagrams commonly used in optical observations. Each diagram contains the 3057 points already discussed in Sections 4.2.3 and 4.2.4. Areas labelled ‘H II regions’, ‘SNRs’ and ‘PNe’ were all reproduced according to Figs 1–3 of Sabbadin et al. (1977). Long-dashed lines in Fig 13(a) and 14(a) indicate the lower and upper

limits for  $[\text{S II}] \lambda 6716/[\text{S II}] \lambda 6731$  that provide finite values of electron densities  $\rho$  given a constant temperature of 7400 K in IC 1805 (see Section 4.2.3).

In all three diagrams, blue crosses are used to represent points found (in majority) within the ‘H II regions’. The relatively high number of crosses is not surprising for IC 1805, already catalogued as an H II region. A certain fraction of the sample, however, falls outside this area. These points are symbolized as red filled circles and point approximately towards the ‘SNRs’ area, hence suggesting evidence for shock excitation in the targeted ISM volume. This will be discussed in Section 5.2. Out of the 3057 points retained for this study, respectively 134 (4.4 per cent), 67 (2.2 per cent) and 84 (2.7 per cent) are displayed as red filled circles in Figs 12(a)–14(a).

Panels (b) of Figs 12–14 provide the spatial distribution of all crosses (shown as blue dots) and circles (shown as red dots) displayed in the diagnostic diagram of their respective panel (a). As in Fig. 10(b), a black-and-white reproduction of Fig. 4 was used. Red dots in Figs 12(b)–14(b) all point at the same areas and reveal that the southern portions of the bright, central structure ( $\delta_{2000} < 61^\circ 26' 30''$ ) may encompass material subject to ionization by shocks.

## 5 DISCUSSION

### 5.1 The $[\text{N II}]$ line ratio: deviations from the theoretical value

As demonstrated in Section 4.2.4, values for the  $[\text{N II}] \lambda 6584/[\text{N II}] \lambda 6548$  line ratio above 3.5 and approaching 4 are partially attributed to poorer data quality especially affecting the lower-signal, noisy  $[\text{N II}] \lambda 6548$  Å line (e.g. see Fig. 2). Fig. 11 indicates that the use of profiles whose emission lines are strictly characterized by ‘very’ high S/N (in our case, greater than 20) contributes to attenuate the right tail of the distribution. The asymmetry coefficient

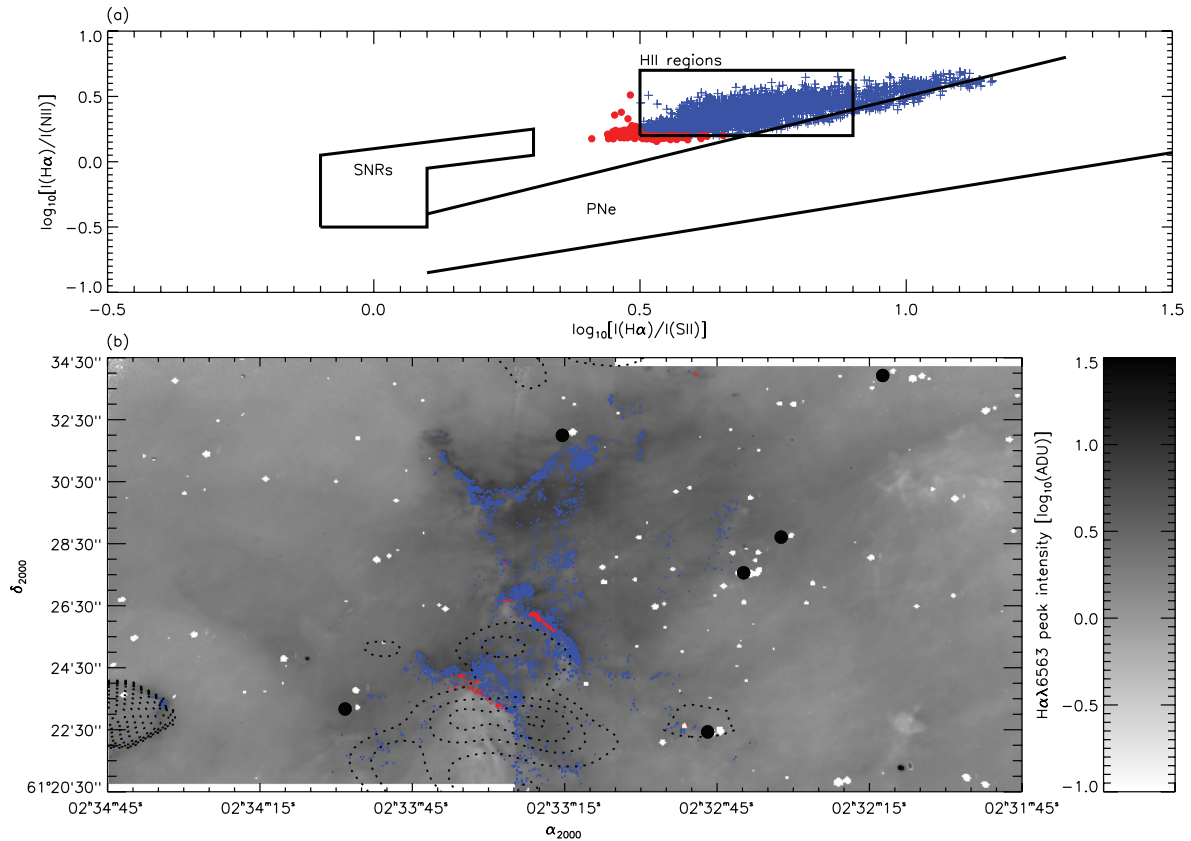


**Figure 12.** Panel (a): diagnostic diagram of the  $\log_{10} [I(\text{H}\alpha)/I([\text{S II}])]$  versus  $\log_{10} [I(\text{H}\alpha)/I([\text{N II}])]$  relation. By definition,  $I(\text{H}\alpha)$  is the peak intensity of the  $\text{H}\alpha$   $\lambda 6563$  Å line while  $I([\text{S II}])$  and  $I([\text{N II}])$  correspond, respectively, to the sum of both lines' peak intensity of the  $[\text{S II}]$  and  $[\text{N II}]$  doublet. While blue crosses indicate photoionization effects typically expected in H II regions, red filled circles deviate towards the shock-dominated regime of SNRs (see the text). Panel (b): spatial distribution of all 3057 points found in panel (a). Blue crosses are represented by blue dots and red filled circles by red dots.

(i.e. skewness) is reduced from roughly 0.4 to 0.2. Consequently, the width of the distribution is statistically narrower while the mean of the histogram slightly varied towards the expected value of  $\sim 3$  for  $[\text{N II}] \lambda 6584 / [\text{N II}] \lambda 6548$ .

None the less, independent of the threshold in S/N used (e.g. 6 or 20), Fig. 11 reveals that the mean  $[\text{N II}] \lambda 6584 / [\text{N II}] \lambda 6548$  ratio exceeds, by a few tenths, the theoretical value. We propose that this could be attributed to a simple statistical effect by which the ratio of transition probabilities between the  $[\text{N II}] \lambda 6548$  Å and  $[\text{N II}] \lambda 6584$  Å transitions does not necessarily equal 3 given the physical properties governing the IC 1805 nebula. Note that the curve of transmission of the interference filter used for data acquisition has not revealed any significant difference between the transmission coefficients of both lines of the  $[\text{N II}]$  doublet.

Table 3.15 of Osterbrock & Ferland (2006) provides, for different ionic transitions, the critical electron density above which collisional de-excitations caused by free electrons become important. This density is estimated at 80 and  $310 \text{ cm}^{-3}$ , respectively, for the  $[\text{N II}] \lambda 6548$  Å and  $[\text{N II}] \lambda 6584$  Å transitions. Hence, for a given electron density between these two values and characterizing the  $\text{N}^+$  volume, the  $[\text{N II}] \lambda 6548$  Å line intensity will be less than expected, a fraction of its flux being 'lost' in (non-radiative) collisional de-excitations. On the other hand, the  $[\text{N II}] \lambda 6584$  Å line intensity will not be affected until densities reach the  $310 \text{ cm}^{-3}$  plateau. Fig. 10(a) provides reasonable evidence for electron densities between 80 and  $310 \text{ cm}^{-3}$  in IC 1805. Hence, a mean  $[\text{N II}] \lambda 6584 / [\text{N II}] \lambda 6548$  ra-

tio of 3.3–3.4 could be explained by a  $[\text{N II}] \lambda 6548$  Å line partially experiencing collisional de-excitations.

From the results presented in Sections 4.2.3 and 4.2.4 (for  $\text{S/N} > 6$ ), Fig. 15 provides the electron densities (as measured from the  $[\text{S II}] \lambda 6716 / [\text{S II}] \lambda 6731$  line ratio; see Fig. 10) versus the  $[\text{N II}] \lambda 6584 / [\text{N II}] \lambda 6548$  line ratio (see Fig. 11) relation. Each  $\rho - ([\text{N II}] \lambda 6584 / [\text{N II}] \lambda 6548)$  pair is represented by a black cross. For each bin of  $10 \text{ cm}^{-3}$  between 10 and  $500 \text{ cm}^{-3}$ , the mean  $[\text{N II}] \lambda 6584 / [\text{N II}] \lambda 6548$  line ratio is displayed as a red filled square. A standard linear regression (Bevington 1969, chapter 4) was applied to the filled-square sample, in the  $80\text{--}310 \text{ cm}^{-3}$  interval, and is displayed as the dashed green line. The value of each bin was adequately weighted in the regression, i.e. bins with large numbers of crosses were given a more important statistical weight.

A clear, monotonic increase of the  $[\text{N II}] \lambda 6584 / [\text{N II}] \lambda 6548$  line ratio with increasing densities would be expected as the  $[\text{N II}] \lambda 6548$  Å line becomes more and more affected by collisional de-excitations (i.e. decreases in intensity). As expected, the linear relation shows a positive slope although its value, very close to 0, largely suggests no correlation at all. Indeed, the quality of the linear fit is relatively poor with a correlation coefficient of 0.35. Hence, we believe that no conclusion can be drawn from Fig. 15. Two possibilities are however provided in order to explain such behaviour.

First, note that the uncertainties are relatively large for both parameters investigated. The mean uncertainty for the  $[\text{N II}] \lambda 6584 / [\text{N II}] \lambda 6548$  line ratio is 0.17, while typical uncertainties for the

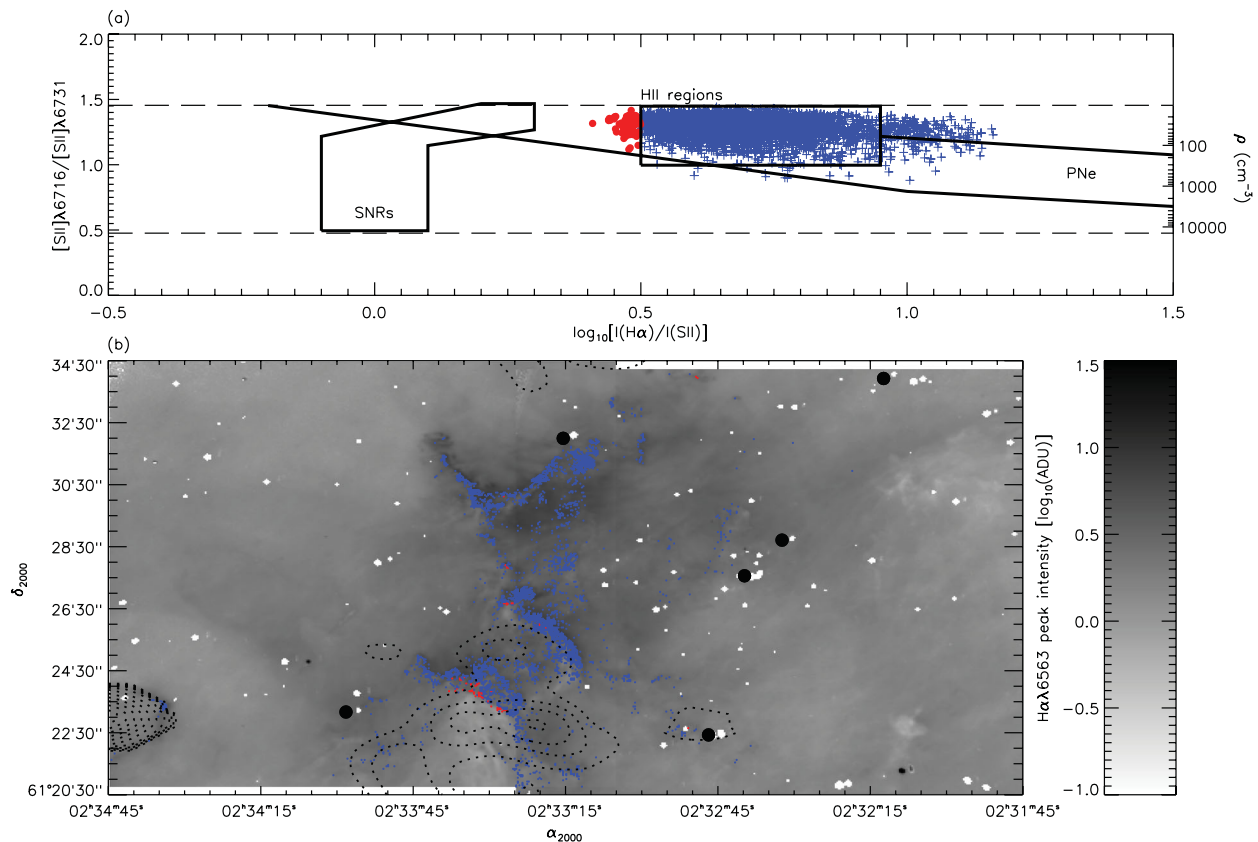


**Figure 13.** Panel (a): diagnostic diagram of the  $\log_{10} [I(\text{H}\alpha)/I([\text{S II}])]$  versus  $[\text{S II}] \lambda 6716/[\text{S II}] \lambda 6731$  line ratio relation. The right-hand ordinate indicates the correspondence between  $[\text{S II}]$  line ratios and electron densities  $\rho$  as provided by our IDL adaptation of the Fivel FORTRAN procedure. Panel (b): spatial distribution of all preserved points. More details are provided in the caption of Fig. 12.

electron-density measurements  $\rho$  are provided in the last paragraph of Section 4.2.3. The poor correlation of the linear fit in Fig. 15 could be attributed to large error bars.

Moreover, the absence of a well-defined correlation between  $\rho$  and  $[\text{N II}] \lambda 6584/[\text{N II}] \lambda 6548$  would not be surprising if the  $\text{N}^+$  and  $\text{S}^+$  material is not perfectly co-spatial in the vicinity of Melotte 15. Given a difference of more than 4 eV between the ionization potentials of neutral nitrogen and sulphur, it can be assumed that the electron densities, computed from the  $[\text{S II}]$  doublet, may not reflect accurately the physical conditions prevailing in the  $\text{N}^+$  ionic volume. Therefore, the  $\rho$  versus  $[\text{N II}] \lambda 6584/[\text{N II}] \lambda 6548$  diagram of Fig. 15 could be an interesting diagnostic tool although our data set may not provide the appropriate spectral information to reliably construct such a diagram. Alternatively, given the first ionization potential of nitrogen (14.5 eV) and oxygen (13.6 eV), the  $[\text{O II}] \lambda 3726/[\text{O II}] \lambda 3729$  line ratio would likely give a more accurate indication of the density behaviour inside the  $\text{N}^+$  volume.

## 5.2 Shock excitation in IC 1805

Panels (a) of Figs 12–14 reveal that a large fraction of the nebular-gas content in the vicinity of the Melotte 15 star cluster appears to be dominated by photoionization, typical of standard  $\text{H II}$  regions. However, points identified outside the expected regime for  $\text{H II}$  regions and located near the ‘SNRs’ area demand to be closely investigated (see Section 4.2.5). In all three figures, these are symbolized as red filled circles and potentially indicate the presence

of shocks in the targeted nebular volume. These areas of our FOV, suggesting shock excitation, are identified as red dots in panels (b) of these figures.

However, at this point, shock excitation in IC 1805 remains highly hypothetical. This is somewhat surprising considering the presence of relatively massive stars in Melotte 15 and their associated strong stellar winds (see Section 2). In order to deeply investigate the impact of shock excitation in IC 1805, we assume that, if present, the shock-excited ionized material is relatively confined and localized along the line of sight, i.e. considering the imposing dimensions of the large  $\text{H II}$  region (e.g. Lagrois & Joncas 2009a,b), the interface between compressive shocks and the surrounding ISM could be several times smaller than the size of the nebula itself. This said, the expected spectral signature of shock excitation could be strongly diluted by photoionized foreground/background material.

### 5.2.1 Central structure

A total of 2378 out of 3057 emission-line profiles retained for this study are directly associated with the bright, central structure clearly visible in Fig. 8. The strong emission of its ionized component (see peak intensities in Figs 3–7) and therefore the quality of the gathered signal make this structure, surrounded by the most massive stars of the Melotte 15 cluster, the ideal feature in our quest for shock excitation in central IC 1805.

First, a series of four weaker portions (in gas emission), specifically surrounding the central structure, were selected. Each of



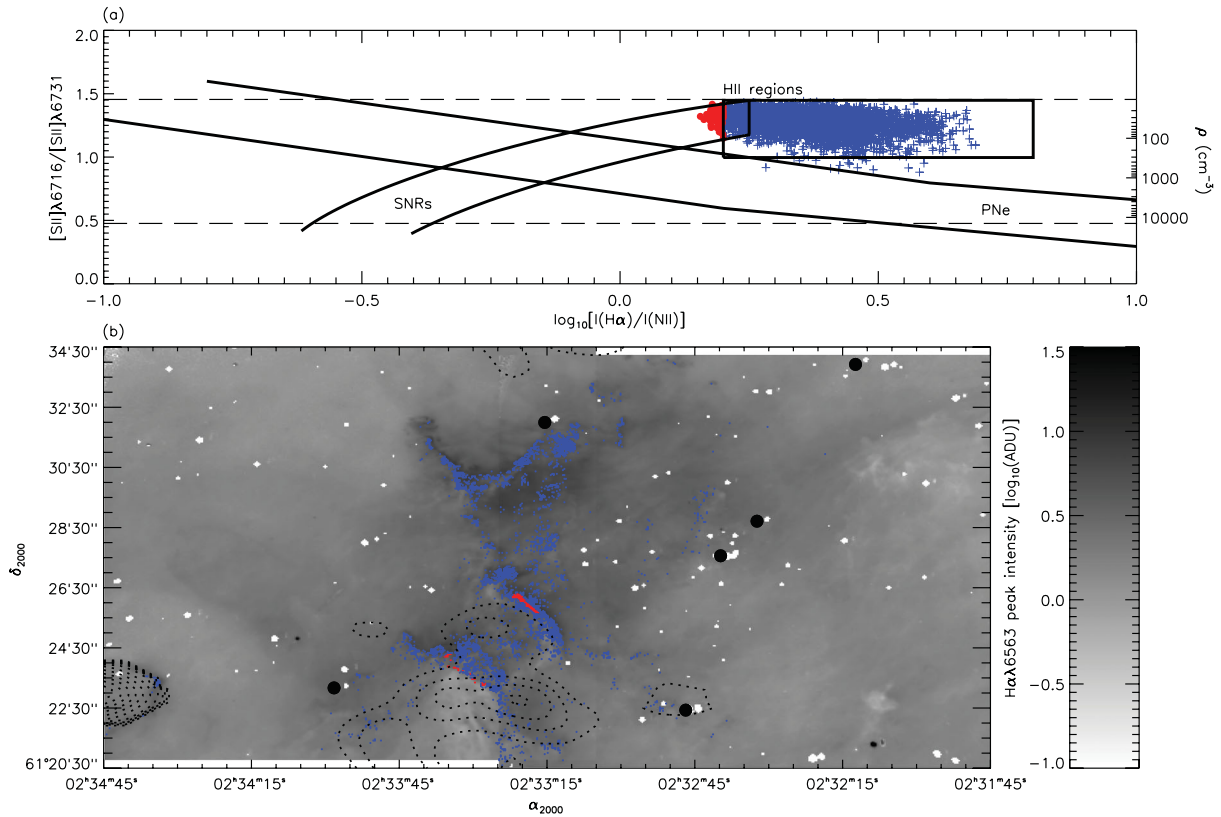


**Figure 14.** Panel (a): diagnostic diagram of the  $\log_{10} [I(\text{H}\alpha)/I(\text{N II})]$  versus  $[\text{S II}] \lambda 6716/[\text{S II}] \lambda 6731$  line ratio relation. Panel (b): spatial distribution of all preserved points. More details are provided in the captions of Figs 12 and 13.

these portions was spatially binned into a single  $1 \times 1 \times 249$  (spatial  $\times$  spatial  $\times$  channels) emission-line profile.<sup>2</sup> For each of the 2378 spectra selected and investigated in this subsection, the corresponding foreground/background emission was approximately recovered using a linear combination of these four  $1 \times 1 \times 249$  profiles. Each of the four linear coefficients was weighted via the inverse of the distance separating the targeted pixel from the center of the corresponding weaker portion (e.g., the larger this distance is, the smaller is the corresponding linear coefficient and, therefore, the smaller is the statistical impact of this weaker zone on the computation of the foreground/background spectral signature at the position of this given pixel). Hence, a unique foreground/background spectrum is constructed for each of the 2378 points (see below) although neighbour pixels have (as it should be) foreground/background material with very similar spectral signatures (i.e. roughly identical linear coefficients).

The subtraction of the foreground/background emission obviously had a certain incidence on the S/N of the resulting profiles, the peak intensity of all five lines being reduced in the subtracting process. Still following all conditions listed in Section 4.2.2, out of 2378 emission-line profiles, 2229 were said to ‘survive’ the procedure. Figs 16(a) and (b) present the  $\log_{10} [I(\text{H}\alpha)/I(\text{S II})]$  versus  $\log_{10} [I(\text{H}\alpha)/I(\text{N II})]$  diagnostic diagram for these 2229 points, respectively, before and after the subtraction of the foreground/background material. Fig. 16(a) is obviously a subset

of Fig. 12(a) and uses the same symbol definitions (see Section 4.2.5). Note that each point preserves its original symbol, shape (cross/circle) and colour (blue/red), from Figs 16(a) to (b).

In Fig. 16(a), 2109 points are displayed as blue crosses while 120 are symbolized as red filled circles, being located close but outside the lower-left corner of the ‘H II regions’ area. Note that 134 points were displayed as red circles in Fig. 12(a) (see Section 4.2.5): 14 of those points were not considered here, either being not associated with the central structure or have simply failed to fulfil the conditions of Section 4.2.2 following the subtracting process discussed above.

In Fig. 16(b), a tail precisely directed towards the ‘SNRs’ area appears as numerous points migrate out of the ‘H II regions’ area. Recent surveys (e.g. Riesgo & López 2006; Frew & Parker 2010) have shown that the boundaries of the different areas circumscribed in the diagnostic diagrams used here could be slightly modified with respect to the first work carried out by Sabbadin et al. (1977). It appears that the lower and upper limits, in the parameter space, for each regime are still uncertain to this day. We therefore chose to arbitrarily redefine (or expand) the zone of shock excitation for each relation investigated. For example, in the  $\log_{10} [I(\text{H}\alpha)/I(\text{S II})]$  versus  $\log_{10} [I(\text{H}\alpha)/I(\text{N II})]$  relation, the hatched area in the lower-left corner of Fig. 16(b) was, from now on, used to separate gas columns (i.e. pixels) likely enclosing post-shocked material from those for which photoionization effects appear to primarily dominate. Now, 509 points out of 2229 suggest evidence for potential shock excitation in the direct vicinity of the Melotte 15 cluster. The tail is formed of both blue crosses and red circles, indicating that Fig. 16(a) alone would not be sufficient in order to precisely pinpoint those sections

<sup>2</sup> The spatial binning of numerous emission-line profiles into a single one flattens out noise fluctuations. Therefore, the resulting spectrum is of very high quality.

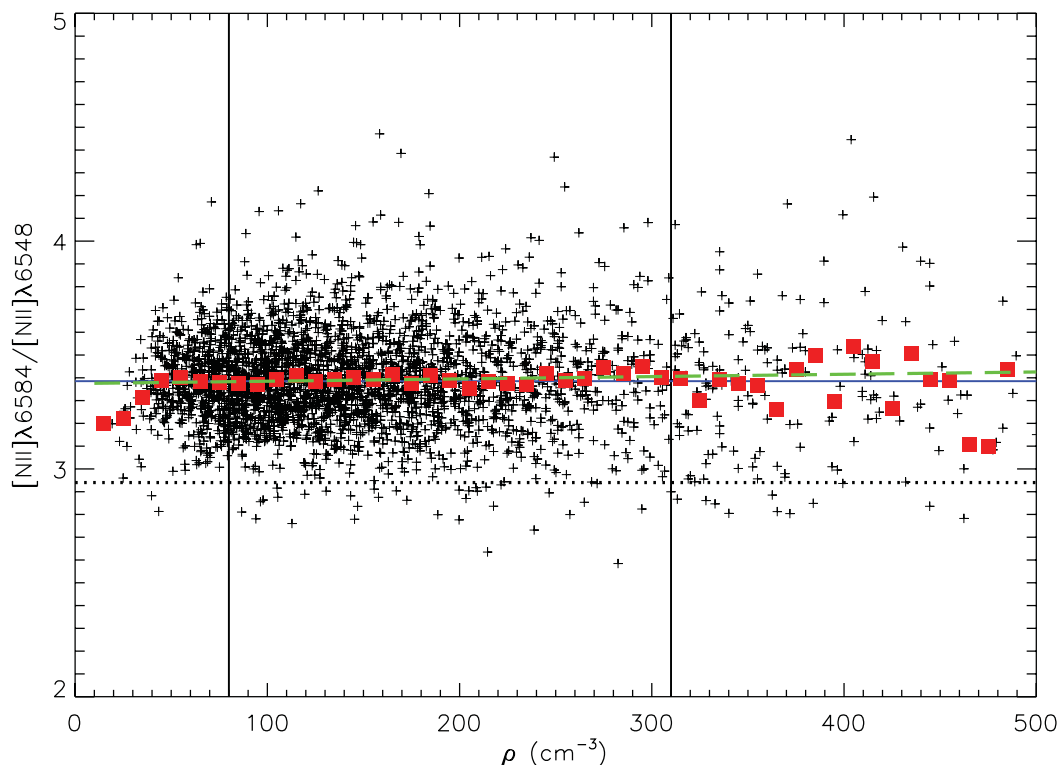


**Figure 15.** Diagram of the mean electron density ( $\rho$ ) versus  $[\text{N II}] \lambda 6584/[\text{N II}] \lambda 6548$  line ratio relation. The horizontal dotted line indicates the theoretical value of the  $[\text{N II}] \lambda 6584/[\text{N II}] \lambda 6548$  ratio as predicted in a low-density regime. The horizontal regular line marks the mean  $[\text{N II}] \lambda 6584/[\text{N II}] \lambda 6548$  ratio retrieved from Fig. 11 (regular-line distribution). The vertical regular lines isolate the 80–310  $\text{cm}^{-3}$  interval in densities where collisional de-excitations are expected to impact the  $[\text{N II}] \lambda 6584$  Å line while the  $[\text{N II}] \lambda 6584$  Å line remains theoretically unaffected (see the text). Red filled squares correspond to the mean  $[\text{N II}] \lambda 6584/[\text{N II}] \lambda 6548$  ratio observed for each bin of 10  $\text{cm}^{-3}$  in densities. The dashed green line indicates the linear fit to the sample of filled squares found between 80 and 310  $\text{cm}^{-3}$ . Large fluctuations of the filled square symbols at high densities ( $\rho \gtrsim 350 \text{ cm}^{-3}$ ) result from low amounts of points (black crosses) within each bin.

of the central structure revealing (or hiding) a well-defined signature of ionization by shocks. Fig. 17(a) provides the post-subtraction spatial distribution of all points found in Fig. 16(b). Points found in the hatched area of the lower-left portion of the diagram are coloured in red. Others, still associated with the ‘H II regions’ area, hence suggesting photoionization effects, are in blue.

Similar exercises were carried out using the corresponding subsets for Figs 13(a) and 14(a) although we will simply provide the results here. The zone of shock excitation was, respectively, for both figures, redefined by  $\log_{10} [\text{I}(\text{H}\alpha)/\text{I}(\text{S II})] < 0.3$  and  $\log_{10} [\text{I}(\text{H}\alpha)/\text{I}(\text{N II})] < 0.2$ , and also bordered by the two long-dashed lines (i.e. lower and upper limits on  $[\text{S II}] \lambda 6716/[\text{S II}] \lambda 6731$ ).

For the  $\log_{10} [\text{I}(\text{H}\alpha)/\text{I}(\text{S II})]$  versus  $[\text{S II}] \lambda 6716/[\text{S II}] \lambda 6731$  diagram, while only 54 out of 2229 points were being found initially outside the ‘H II regions’ area prior to the subtraction of the foreground/background material, 509 points have shown  $\log_{10} [\text{I}(\text{H}\alpha)/\text{I}(\text{S II})] < 0.3$  afterwards. Again, as in Fig. 16(b), evidence for shocks appears for both blue crosses and red filled circles. Fig. 17(b) gives the spatial distribution of the post-subtraction points. One clearly sees the perfect correspondence between Figs 17(a) and (b), i.e. using two distinct diagrams the same points, which suggest shock excitation, are extracted.

For the  $\log_{10} [\text{I}(\text{H}\alpha)/\text{I}(\text{N II})]$  versus  $[\text{S II}] \lambda 6716/[\text{S II}] \lambda 6731$  relation, the situation is more complex as the ‘SNRs’ and ‘H II regions’ areas overlap in the diagnostic tools (see Fig. 14a). The removal of the foreground/background material has led to 1419

points displaying  $\log_{10} [\text{I}(\text{H}\alpha)/\text{I}(\text{N II})]$  values below 0.2, although roughly half of these remain very close to the ‘H II regions’ area. For the  $\log_{10} [\text{I}(\text{H}\alpha)/\text{I}(\text{N II})]$  versus  $[\text{S II}] \lambda 6716/[\text{S II}] \lambda 6731$  relation, Fig. 17(c) gives the spatial distribution of the post-subtraction points using the same colour code as in Figs 17(a) and (b).

Combining the post-subtraction results for all three diagrams allows us to spatially identify those sections on the plane of the sky that suggest shock excitation. Fig. 17(d) combines all results found in Figs 17(a–c). Red dots that can be found in all three post-subtraction diagnostic diagrams are again coloured in red. These points targeted regions with high probability of shock excitation in central IC 1805. The red dots that can only be found in Fig. 17(c) are coloured in green in Fig. 17(d). These can be referred to as interesting candidates for shock excitation, although two out of three diagrams have failed to identify them. Blue dots in all three post-subtraction diagnostic diagrams are coloured in blue and identify the zones, mostly located near the northern tip of the bright ionized feature, where photoionization clearly dominates.

Shock-dominated material seems to prevail along the southern portion of the central structure, directly exposed to the stellar winds and currently eroded by the ionizing flux of the two most massive stars identified in Melotte 15 (identified by black arrows in Fig. 17d). These are catalogued by Massey et al. (1995) as HB 15558 and HB 15570, two evolved O4III(f) ( $\alpha_{2000} = 02^{\text{h}}32^{\text{m}}43^{\text{s}}$ ,  $\delta_{2000} = 61^{\circ}27'22''$ ) and O4If ( $\alpha_{2000} = 02^{\text{h}}32^{\text{m}}50^{\text{s}}$ ,  $\delta_{2000} = 61^{\circ}22'42''$ ) stars, respectively. Ionization by shocks clearly dominates the bright ionized gas at the

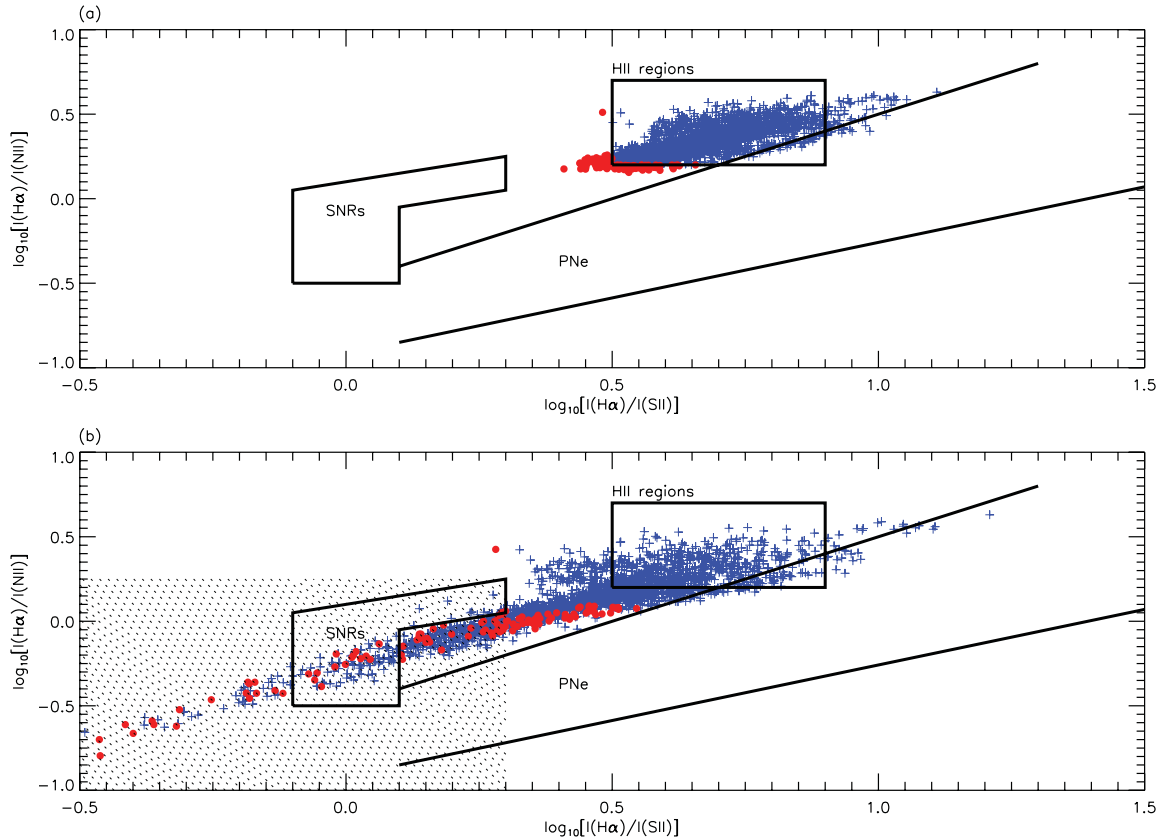


**Figure 16.** Panel (a): diagnostic diagram of the  $\log_{10} [I(\text{H}\alpha)/I([\text{S II}])]$  versus  $\log_{10} [I(\text{H}\alpha)/I([\text{N II}])]$  relation for points strictly associated with the bright, central structure and prior to the subtraction of the foreground/background material (see the text). Definitions for blue crosses and red filled circles are the same as in Fig. 12(a). Panel (b): diagnostic diagram of the  $\log_{10} [I(\text{H}\alpha)/I([\text{S II}])]$  versus  $\log_{10} [I(\text{H}\alpha)/I([\text{N II}])]$  relation for points strictly associated with the bright, central structure and following the subtraction of the foreground/background material (see the text). Each point kept its original symbol used in panel (a). The hatched area roughly indicates the zone in the parameter space where already catalogued shock-dominated objects can be found.

periphery of the weak molecular material found in the southernmost portion of our FOV. Our results reveal that shock excitation appears to be correlated with bright ionized material, suggesting high electron densities if we assume the nebula to be optically thin to the ionic light. This would then be easily correlated to the compressive nature of the hypothetical shocks.

Extracting the electron densities  $\rho$  for all 1419 points (rather in red or green in Fig. 17d) yields the blue-line histogram of Fig. 10(a). Its mean is estimated at  $125^{+70}_{-50} \text{ cm}^{-3}$ , slightly below the mean value previously derived for the whole sample of 3057 emission-line profiles retained for this work (see Section 4.2.3). This hardly makes sense considering the compression expected from shock waves. However, keeping in mind that the subtraction of, what we referred to as, the foreground/background material was required in order to spectrally detect evidence for shock excitation in IC 1805, it seems logical that the same procedure should be applied in the extraction of the electron densities specifically associated with the shocked, ionized component. Using the 1419 post-subtraction emission-line profiles that showed evidence for shock excitation, the corresponding electron densities ( $\equiv \rho_{\text{shock}}$ ) were computed following the method described in Section 4.2.3. The red histogram in Fig. 10(a) reveals the distribution obtained for  $\rho_{\text{shock}}$ . The mean electron density along the line of sight at the position of shocks is estimated at  $175 \text{ cm}^{-3}$ , a mean roughly  $20 \text{ cm}^{-3}$  greater than what was found for the black histogram in Fig. 10(a). This suggests, as expected, that the foreground/background material probably occupies, near

Melotte 15, a large volume filled with a very diffuse ionized component. This tenuous material undoubtedly contributes to attenuate the ionic emission of high-density condensations along the line of sight.

Using the 1419 spectra of the foreground/background emission, we extracted to corresponding densities ( $\equiv \rho_{\text{diffuse}}$ ). As expected, this tenuous component has a mean electron density along the line of sight of  $25 \text{ cm}^{-3}$ . The distribution shows a narrow width of roughly  $15 \text{ cm}^{-3}$ , which reflects the homogeneity (in density) of the foreground/background material over the entire spatial extent of the central, ionized structure. Fig. 18 shows the distribution of the pixel-to-pixel compression factor, i.e.  $\rho_{\text{shock}}/\rho_{\text{diffuse}}$ . All remaining 1419 points formed the black histogram. The mean compression is estimated at 8.5, although the histogram is clearly dominated by values of  $\rho_{\text{shock}}/\rho_{\text{diffuse}}$  below 5. As expected, the compression factor is always greater than 1. Sub-distributions in green and red give the compression factor for the green and red dots, respectively, obtained in Fig. 17(d). The green histogram, formed of points suggesting possible shock excitation, is very similar statistically to the black distribution with a mean of 7.5. The red histogram, this time formed of points with a high probability of shock excitation, is slightly different, peaking at a greater  $\rho_{\text{shock}}/\rho_{\text{diffuse}}$  value. Its mean is estimated slightly above 10, i.e. the points (red in Fig. 17d) where, we believe, shocks may certainly dominate seem to be characterized by greater compression effects with respect to points (green in Fig. 17d) where the presence of shocks appears less obvious.

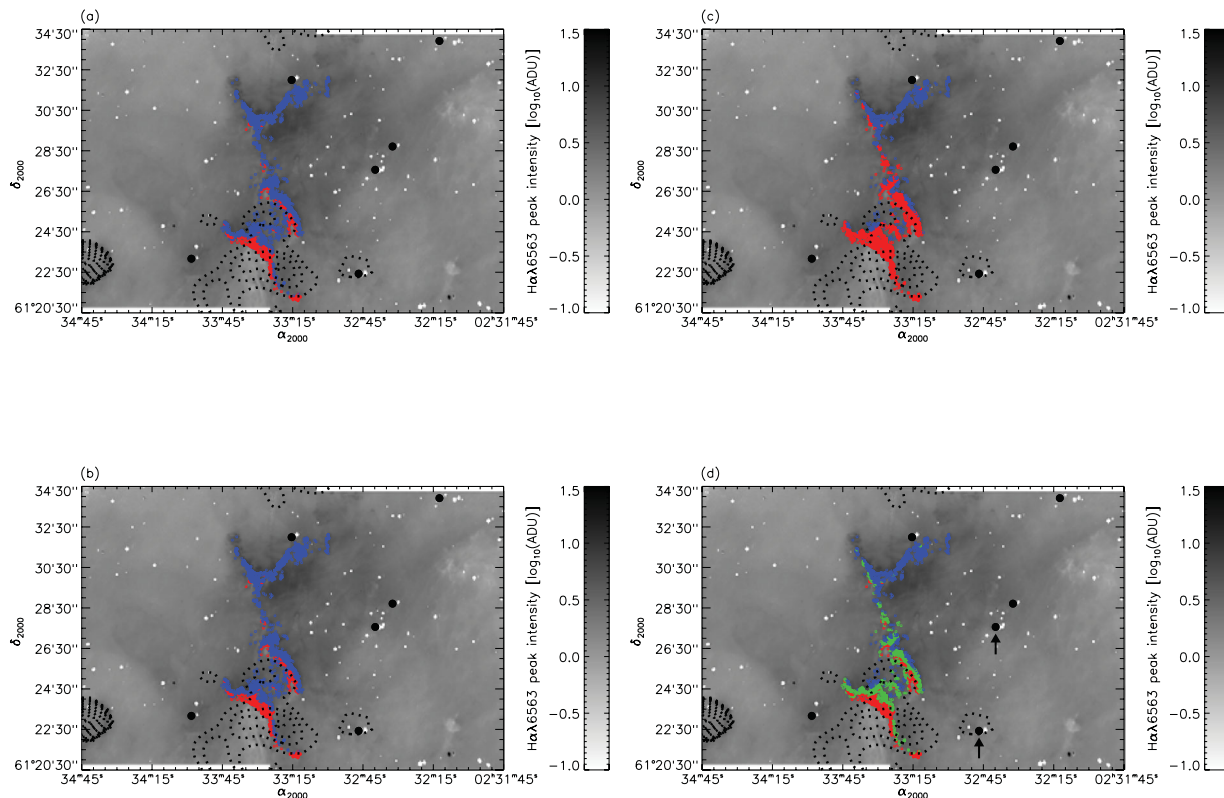


**Figure 17.** Peak-intensity maps of the  $H\alpha$   $\lambda 6563$  Å ionic transition in IC 1805 (see the caption of Fig. 4). Panel (a): obtained from the post-subtraction  $\log_{10} [I(H\alpha)/I([S II])]$  versus  $\log_{10} [I(H\alpha)/I([N II])]$  relation, the specific lines of sight, associated with the bright, central structure and suggesting evidence for shock excitation, are represented in red. Blue dots indicate the position where the ionized material is most likely dominated by photoionization effects. Panel (b): the same as panel (a) for the  $\log_{10} [I(H\alpha)/I([S II])]$  versus  $[S II] \lambda 6716/[S II] \lambda 6731$  line ratio relation. Panel (c): the same as panel (a) for the  $\log_{10} [I(H\alpha)/I([N II])]$  versus  $[S II] \lambda 6716/[S II] \lambda 6731$  line ratio relation. Panel (d): combination of panels (a)–(c). Red dots present in all first three panels are again coloured in red. Dots coloured in red in panel (c) but blue in panels (a) and (b) are coloured in green. Blue dots present in all first three panels are again coloured in blue. The two most massive O-stars in the Melotte 15 cluster are identified by the black arrows (see the text).

For adiabatic jump conditions, Rankine–Hugoniot relations indicate a compression factor of precisely 4 between pre- and post-shocked gas (Henny, Lamers & Cassinelli 1999, chapter 12). The relatively large widths of the distributions displayed in Fig. 18 indicate that isothermal shocks may dominate. Also, the fact that forbidden lines such as  $[N II]$  and  $[S II]$  are detected favours radiative cooling and therefore non-adiabatic effects (although these lines most likely originate from ionized material trapped in the cooling, shocked outer shell and therefore may not be related to the wind-blown bubble’s current state of expansion, i.e. energy- or momentum-driven). Theoretically, for an isothermal shock (Dyson & Williams 1980, chapter 6), the compression factor corresponds to the square of the shock’s Mach number,  $M_0$  (see the abscissa in Fig. 18). Therefore, for a speed of sound of  $10 \text{ km s}^{-1}$  in the  $H^+$  medium (in agreement with our choice of 7400 K for the electron temperature in IC 1805; see Section 4.2.3), shocks with typical velocities between 15 and  $30 \text{ km s}^{-1}$  (i.e.  $M_0^2 = 2\text{--}10$ ) may have led to shock excitation near Melotte 15. This is in agreement with typical expansion velocities found for wind-blown bubbles (see Section 1). Shock velocities up to  $50 \text{ km s}^{-1}$  (i.e.  $M_0^2 \sim 25$ ) are also found, although such dynamics is certainly peculiar. Note, however, that the compression measured here could be an upper limit since photo-eroded gas located in the molecular cloud’s envelope, rather than the diffuse foreground/background component, may act as pre-shocked material. The cloud’s envelope is expected to be, at least, a few tens

of particles per  $\text{cm}^3$  denser than typical values found for  $\rho_{\text{diffuse}}$  in this work (Rathborne et al. 2009).

Assuming a coplanar geometry, roughly 3–4 pc separate the most massive star of the Melotte 15 cluster and the central, ionized structure. Using the standard model for expanding wind-blown bubbles (Weaver et al. 1977), the distance reached by a given bubble’s post-shocked shell can be estimated from the mechanical luminosity of the winds [ $L_w = (\dot{M}_w v_\infty^2)/2$ ], the density of the pre-shocked medium ( $\rho_{\text{diffuse}}$ ) and the total time during which winds have been blown by the central star ( $t_w$ ). Given  $t_w = 2.5 \text{ Myr}$ , the age of the Melotte 15 cluster (see Section 2), we expect that two massive giant and supergiant O4 stars have left just very recently the main-sequence branch. Therefore, for the calculations to follow, these were treated as O4V stars. From different studies proposing typical mass-loss rates and terminal velocities with respect to spectral types (Prinja, Barlow & Howarth 1990; Lamers et al. 1999; Markova et al. 2004),  $\dot{M}_w$  and  $v_\infty$  were, respectively, estimated at  $5 \times 10^{-6} M_\odot \text{ yr}^{-1}$  and  $3000 \text{ km s}^{-1}$  for standard O4V stars. Given  $\rho_{\text{diffuse}} \sim 25 \text{ cm}^{-3}$  (see above), nebular material found within 15–20 pc of Melotte 15 is likely to have been previously disrupted by stellar winds emanating from the current cluster. This was calculated assuming radiative (non-adiabatic) shocks (Lozinskaya 1992, equation 13.5). Given that interstellar shocks are usually adiabatic at the earliest times of the expansion, the non-radiative model yields a distance of roughly 40 pc in the vicinity of Melotte 15 (Lozinskaya 1992, equation 13.9). Both distances exceed the extent of our FOV



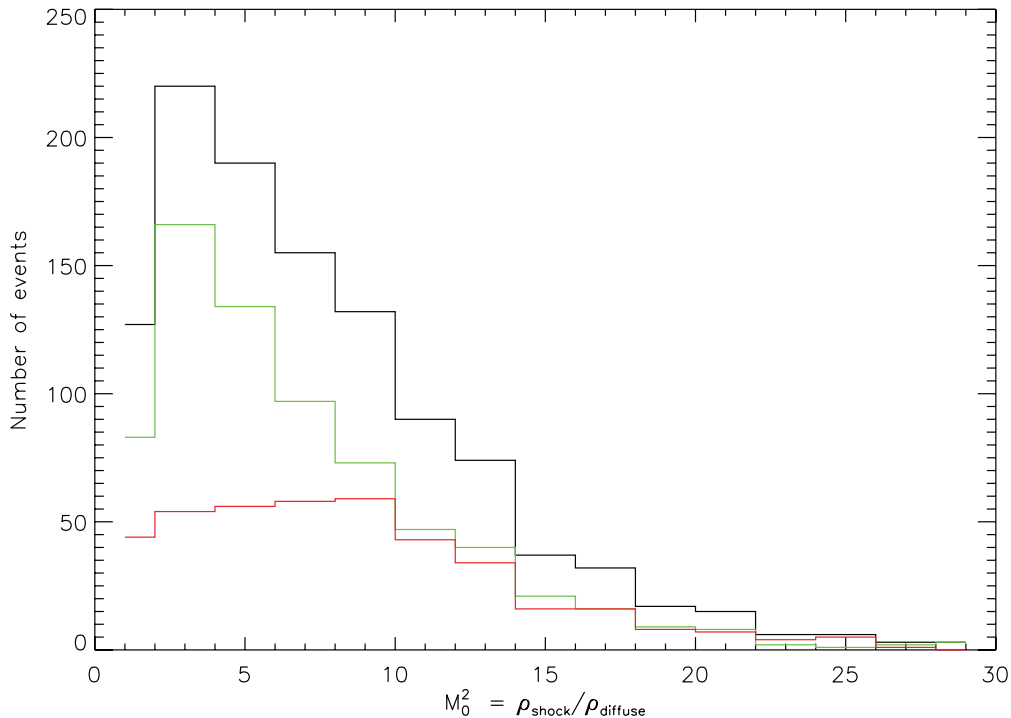


**Figure 18.** Histogram of the compression factor for points, associated with the central structure, revealing post-subtraction evidence for shock excitation (red and green dots in Fig. 17d). The parameter  $\rho_{\text{shock}}/\rho_{\text{diffuse}}$  corresponds, pixel-to-pixel, to the ratio between the electron density computed from the  $[\text{S II}] \lambda 6716/[\text{S II}] \lambda 6731$  line ratio following the subtraction of the foreground/background material and the electron density of the diffuse component retrieved from the foreground/background spectrum (see the text). The green and red distributions are subsets of the black histogram and correspond, respectively, to the sets of green and red dots found in Fig. 17(d).

( $15 \times 9 \text{ pc}^2$ ) and support the fact that shocks, attributed to the current star cluster, have had sufficient time to reach the bright structure in central IC 1805.

### 5.2.2 Shock excitation in other zones of the nebula

Besides the bright, central structure observed near the most massive stars of the Melotte 15 cluster, our FOV mostly reveals diffuse ionized gas, partially obscured by interstellar dust. However, two structures are none the less detected, particularly well defined in  $\text{H}\alpha$  (see Section 4.1). In order to investigate the presence of shock excitation in other portions of our FOV, an approach similar to that carried out in Section 5.2.1 is used here on these two features.

**5.2.2.1 South-east CO fragment.** Fig. 19(a) reveals the shape of the ionization front observed at the periphery of the CO fragment found in the south-east portion of our FOV (see Fig. 8). As in Figs 3–9, north is up and east is to the left. The molecular feature is well defined in the millimetre regime and its western side shows signs of erosion by the nearby star cluster.

The ionized gas associated with the ionization front was first circumscribed while weaker areas near the bright  $\text{H}^+$  feature were selected and used to extract the foreground/background spectrum. In order to obtain a post-subtraction sample containing a sufficient number of emission-line profiles, only the first condition of Section 4.2.2 was used. Therefore, results presented here should be cautiously interpreted.

Prior to the subtraction, all points were initially found inside the ‘ $\text{H II}$  regions’ area of the  $\log_{10} [\text{I}(\text{H}\alpha)/\text{I}([\text{S II}])]$  versus  $\log_{10} [\text{I}(\text{H}\alpha)/\text{I}([\text{N II}])]$  diagnostic diagram and black filled circles

were used as symbols. Fig. 19(b) displays the diagram for post-subtraction spectra only. These results reveal, as in Section 5.2.1, that points are displaced towards the shock-dominated ‘SNRs’ area, although the tail is much less developed when compared to Fig. 16(b). No post-subtraction point actually enters the hatched area defined earlier.

Shock excitation hence appears to have played a much more minor role in the ionization of this cloud’s envelope when compared to the central structure of our FOV. The apparent shape of the ionization front indicates that the ionizing sources are located behind the molecular cloud (see Section 4.1). Using kinematical information retrieved from the photoevaporated material in the vicinity of the cloud, Lagrois & Joncas (2009a) suggested that an appreciable distance could exist between the CO fragment and the Melotte 15 cluster (see their fig. 11 and associated flow G). Hence, large distances could signify here that stellar-wind shocks may have been partially dissipated before they could reach the molecular cloud. Shock excitation is therefore likely measurable only within a certain distance of the shock sources, i.e. stars with strong stellar winds in our case. Obviously, the stronger the shocks are, the greater this corresponding distance is. We reiterate that only the first 15–40 pc in the vicinity of Melotte 15 may have been disrupted by stellar winds (see Section 5.2.1). At this point, the strongest wind shocks (fuelled up by the O4 stars) would have receded to the subsonic regime with velocities between 4 and  $9 \text{ km s}^{-1}$  depending on the model used (radiative or non-radiative, respectively). If, by any chance, the molecular fragment found near the south-eastern boundary of our FOV is located relatively far from the ionizing sources ( $\gtrsim 15 \text{ pc}$ ), this could explain the apparent absence of strong, compressive shocks at its periphery.

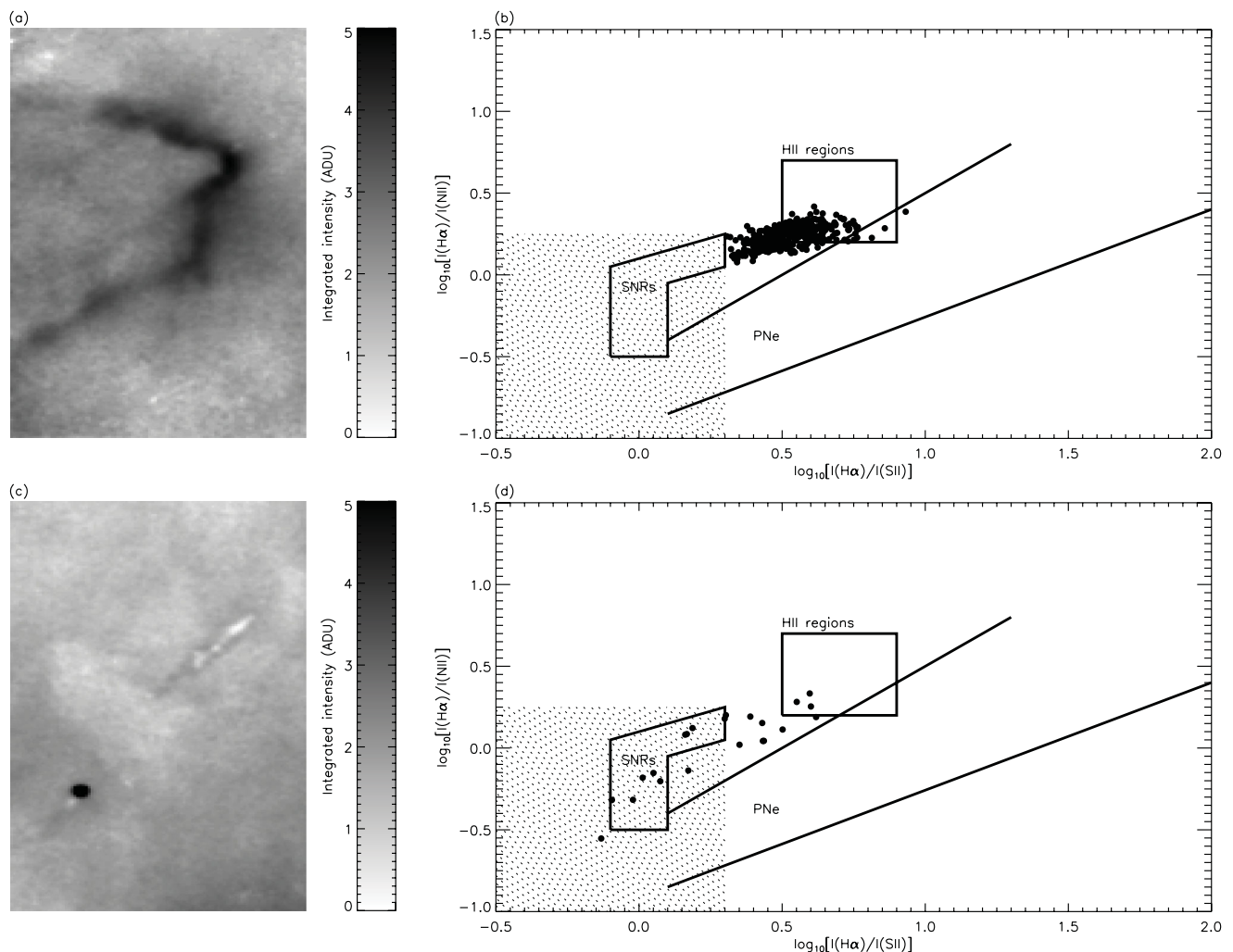


**Figure 19.** Investigating the presence of shock excitation in other portions of IC 1805. Panel (a): integrated intensity of the H $\alpha$  ionic transition near the CO fragment, detected by the FCRAO survey, and located in the south-east portion of our FOV (see Section 4.1). Panel (b): diagnostic diagram of the  $\log_{10} [I(\text{H}\alpha)/I(\text{S II})]$  versus  $\log_{10} [I(\text{H}\alpha)/I(\text{N II})]$  relation for points associated with the bright ionization front displayed in panel (a). The diagram is obtained following the subtraction of the foreground/background material (see the text). Panel (c): integrated intensity of the H $\alpha$  ionic transition associated with a cigar-like structure pointing towards a nearby star with strong H $\alpha$  emission. Panel (d): diagnostic diagram of the  $\log_{10} [I(\text{H}\alpha)/I(\text{S II})]$  versus  $\log_{10} [I(\text{H}\alpha)/I(\text{N II})]$  relation for points associated with the cigar-like structure displayed in panel (c). The diagram is obtained following the subtraction of the foreground/background material (see the text). For panels (a) and (c), both maps were processed using the spectral collapse of the initial mosaicked cube in the channel interval of the H $\alpha$   $\lambda 6563$  Å ionic line.

**5.2.2.2 Cigar-like structure.** Fig. 19(c) shows the very tenuous, but well-defined, ionized counterpart of a cigar-like structure pointing towards a nearby star with strong H $\alpha$  emission line. Again, north is up and east is to the left. The star is particularly visible on the left-hand side of Fig. 8 and has been catalogued by Kohoutek & Wehmeyer (1999) as HBH $\alpha$  6211-05 with a V-band magnitude of 14.6 and no known spectral type. Its coordinates are ( $\alpha_{2000} = 02^{\text{h}}34^{\text{m}}10^{\text{s}}.06$ ,  $\delta_{2000} = 61^{\circ}24'35''.7$ ). The elongated feature was briefly introduced in Section 4.1.

Emission in H $\alpha$  and [N II] is detected on the outskirts of the cigar-like feature while its centre appears mostly gas depleted. This overall scheme is particularly similar to what is expected from elephant trunks in H II regions (e.g. Carlqvist, Gahm & Kristen 2003). Shadowing effects caused by a dense neutral globule located in a radiation field allow the warm gas behind it to recombine, which could explain the absence of ionized material at the centre of the elongated structure. The bright ionized rims are formed of photo-

evaporated material created by the erosion of the neutral globule. These flows move away from the ionizing star creating the cigar-like shape.

Both the FCRAO CO(1–0) survey and the Canadian Galactic Plane Survey at 21 cm (Normandeau, Taylor & Dewdney 1997) reveal no indication for either molecular or atomic gas associated with the elongated feature. Theoretically, H $_2$  is expected to constitute the main component of the eroded globule while H I material should result from recombinations in the tail. The whole structure, however, has relatively small angular dimensions ( $45 \times 7$  arcsec $^2$ ), which suggests that emission from the neutral gas could be beam diluted in the low-resolution radio observations.

Theory has suggested that shocks will develop in elephant trunks (Mackay & Lim 2010; Raga, Lora & Smith 2010) although, in first approximation, the  $\log_{10} [I(\text{H}\alpha)/I(\text{S II})]$  versus  $\log_{10} [I(\text{H}\alpha)/I(\text{N II})]$  diagram has shown nothing particular using the first set of Gaussian fits, i.e. all points associated with the

elongated structure are well confined into the ‘H II regions’ area. However, subtracting the foreground/background material yields the diagram displayed in Fig. 19(d). None of the conditions listed in Section 4.2.2 was considered. Only an S/N greater than 3 (sufficiently high to confirm a physical detection; see Section 4.2.2) was required here. Therefore, the results are highly questionable although worth mentioning. The ionized material at the centre of the cigar-like feature being very tenuous (or simply non-existent; see above), all points filling the diagram are found along the external bright rims. Fig. 19(d) reveals that the ‘SNRs’ area of the shock-dominated material is highly favoured, in agreement with the prediction of shock development proposed by the theory.

The particular shape of the elongated structure presented in Fig. 19(c) could be easily mistaken for jets attributed to Herbig–Haro (HH) objects. However, fig. 4(a) of Frew & Parker (2010) indicates the peculiar low intensities of the [N II] lines in HH objects. This leads to a position, for HH objects in the  $\log_{10} [I(\text{H}\alpha)/I(\text{S II})]$  versus  $\log_{10} [I(\text{H}\alpha)/I(\text{N II})]$  diagram, clearly above the ‘SNRs’ area. This said, the diagram in Fig. 19(d) most likely confirms that the cigar-like feature is not part of an HH object in IC 1805. Rather, the elephant-trunk nature suggested here appears very plausible.

## 6 CONCLUSION

The use of the imaging Fourier transform spectrometer SpIOMM allowed us to obtain a series of emission-line profiles of the optical gas in the brightest, central portions of the Galactic IC 1805 H II region. The bandwidth used at data acquisition allowed the simultaneous observations of the H $\alpha$   $\lambda$ 6563 Å, [N II]  $\lambda$ 6548, 6584 Å, and [S II]  $\lambda$ 6716, 6731 Å ionic lines (see Section 3).

The main goal of this work was to investigate the presence of supersonic shock waves attributed to stellar winds in the vicinity of Melotte 15, the current star cluster actually fuelling up the expansion of the IC 1805 nebula. The literature has long suggested that a kinematical detection of stellar winds, in the H II region, might represent a difficult task since the typical expansion velocity of shocked shells could be commonly confused with other dynamical processes revealing similar kinematical behaviours (see Section 1). On the other hand, specific line ratios retrieved from the optical gas may indicate if the presence of ionized material is attributed to standard photoionization or to shock excitation. These line ratios therefore provide a non-kinematical tool for identifying shocks in the nebular volume. Our results are summarized as follows.

I. The [N II]  $\lambda$ 6584/[N II]  $\lambda$ 6548 line ratio genuinely deviates from the theoretical value of 3 (see Section 5.1). Values varying between 2.5 and 4 were commonly found. The distribution of the density measurements has not allowed us to demonstrate that the [N II]  $\lambda$ 6548 Å line could be affected by collisional de-excitations, hence reducing its peak intensity. This scenario remains none the less plausible and could be verified if densities in the N<sup>+</sup> volume could be measured precisely (see Section 5.1). Densities extracted from the [S II]  $\lambda$ 6716/[S II]  $\lambda$ 6731 ratio may not perfectly reflect the conditions prevailing in the N<sup>+</sup> volume if both nitrogen and sulphur are not co-spatial in central IC 1805.

II. The diagnostic diagrams introduced by Sabbadin et al. (1977) indicate, in first approximation, that photoionization most likely dominates in IC 1805 (see Section 4.2.5). This initially holds even for the densest, most emissive structures in our FOV, directly exposed to the radiation fields and stellar winds of the nearby, most massive stars (see Section 5.2).

III. Evidence for shock excitation appears only following the subtraction of the diffuse foreground/background material. This com-

ponent likely occupies a very large fraction of the nebular volume in IC 1805, a volume sufficiently large that, even though being tenuous in nature, the foreground/background material strongly dilutes the signal emanating from shocked condensations along the line of sight. Its mean density is estimated at 25 cm<sup>-3</sup> (see Section 5.2.1).

IV. Oriented on a south–north axis and surrounded by numerous O-stars, a bright, large ionized feature occupies the central area of our FOV. The last, tenuous fragments of an old molecular cloud can be found near its southern portion. Shocks may have contributed to ionize material found in the direct vicinity of the molecular clump, while the northern parts of the ionized feature deprived of molecular emission appear to be largely dominated by photoionization (see Section 5.2.1).

V. The shock-excited ionized gas has a mean density of 175 cm<sup>-3</sup> and the compression factor, between pre- and post-shocked gas, is typically between 2 and 10. For isothermal shocks, this suggests shock velocities between 15 and 30 km s<sup>-1</sup>, in agreement with models describing the expansion of wind-blown bubbles (see Section 5.2.1). Geometrically speaking, given the apparent proximity between the central, ionized structure and the most massive stars of Melotte 15, winds seem to have had sufficient time to reach the structure within a time-scale corresponding to the age of the star cluster (see Section 5.2.1). This gives credence to our assumption that shock excitation can be found in the south-central portions of our FOV.

VI. Points identified with a high probability of shock excitation reveal compression factors typically greater than those points where shocks may be present although less certain (see Section 5.2.1).

VII. Shocks did not seem to have played a major role in the ionization of a molecular cloud’s envelope located in the south-eastern portion of our FOV. This most likely results from the molecular fragment being located too far from the ionizing sources so that (1) shocks induced by stellar winds have not yet reached the cloud or (2) shocks have reached the cloud with velocities too low to initiate shock excitation (see Section 5.2.2.1).

VIII. Shock development was clearly detected on the outskirts of an apparently weak, but well-defined elephant trunk located in the eastern portion of our FOV (see Section 5.2.2.2). This is in agreement with theoretical works developed on such feature typically found in H II regions.

## ACKNOWLEDGMENTS

We thank the Natural Sciences and Engineering Research Council of Canada and the Fonds Québécois de la Recherche sur la Nature et les Technologies, who provided funds for this research project.

DL is grateful to M.-A. Miville-Deschênes and D. J. Marshall, who provided useful IDL routines to carry out data reduction. DL and LD would like to thank B. Malenfant, G. Turcotte and P.-L. Lévesque for technical support during numerous observing nights at the Observatoire du Mont-Mégantic and also A.-P. Bernier and M. Charlebois who provided convenient help during data acquisition. The development of SpIOMM is a collaboration between Université Laval and ABB Bomm.

Finally, we are especially thankful to our referee, Dr Luis Cuesta, for very relevant suggestions that were used to improve the manuscript.

## REFERENCES

- Arsenault R., Roy J.-R., 1988, A&A, 201, 199
- Arthur S. J., Hoare M. G., 2006, ApJS, 165, 283

- Basu S., Johnstone D., Martin P. G., 1999, *ApJ*, 516, 843
- Bernier A.-P., Charlebois M., Drissen L., Grandmont F., 2008, *Proc. SPIE*, 7014, 70147J
- Bevington P. R., 1969, *Data Reduction and Error Analysis for the Physical Sciences*. McGraw-Hill, New York
- Bodenheimer P., Tenorio-Tagle G., Yorke H. W., 1979, *ApJ*, 233, 85
- Carlqvist P., Gahm G. F., Kristen H., 2003, *A&A*, 403, 399
- Charlebois M., Drissen L., Bernier A.-P., Grandmont F., Binette L., 2010, *AJ*, 139, 2083
- De Robertis M. M., Dufour R. J., Hunt R. W., 1987, *J. R. Astron. Soc. Can.*, 81, 195
- Drissen L., Bernier A.-P., Charlebois M., Brière É., Robert C., Joncas G., Martin P., Grandmont F., 2008, *Proc. SPIE*, 7014, 70147K
- Dyson J. E., Williams D. A., 1980, *The Physics of the Interstellar Medium*. Manchester Univ. Press, Manchester
- Frew D. J., Parker Q. A., 2010, *PASA*, 27, 129
- Henny J. G., Lamers L. M., Cassinelli J. P., 1999, *Introduction to Stellar Winds*. Cambridge Univ. Press, Cambridge
- Heyer M. H., Brunt C., Snell R. L., Howe J. E., Schloerb F. P., 1998, *ApJS*, 115, 241
- Joncas G., Roy J.-R., 1984, *ApJ*, 283, 640
- Kohoutek L., Wehmeyer R., 1999, *A&AS*, 134, 255
- Lagrois D., Joncas G., 2009a, *ApJ*, 691, 1109
- Lagrois D., Joncas G., 2009b, *ApJ*, 693, 186
- Lagrois D., Joncas G., 2011, *MNRAS*, 413, 721
- Lamers H. J. G. L. M., Haser S., De Koter A., Leitherer C., 1999, *ApJ*, 516, 872
- Landman D. A., Roussel-Dupré R., Tanigawa G., 1982, *ApJ*, 261, 732
- Llorente de Andrés F., Burki G., Ruiz del Arbol J. A., 1982, *A&A*, 107, 43
- Lozinskaya T. A., 1992, *Supernovae and Stellar Wind in the Interstellar Medium*. AIP, New York
- MacAlpine G. M., Satterfield T. J., 2008, *AJ*, 136, 2152
- MacAlpine G. M., Ecklund T. C., Lester W. R., Vanderveer S. J., 2007, *AJ*, 133, 81
- Mackay J., Lim A. J., 2010, *MNRAS*, 403, 714
- Magrini L., Perinotto M., Corradi R. L. M., Mampaso A., 2003, *A&A*, 400, 511
- Markova N., Puls J., Repolust T., Markov H., 2004, *A&A*, 413, 693
- Massey P., Johnson K. E., DeGioia-Eastwood K., 1995, *ApJ*, 454, 151
- Mellema G., Arthur S. J., Henney W. J., Iliev I. T., Shapiro P. R., 2006, *ApJ*, 647, 397
- Normandeau M., Taylor A. R., Dewdney P. E., 1997, *ApJS*, 108, 279
- Osterbrock D. E., Ferland G. J., 2006, *Astrophysics of Gaseous Nebulae and Active Galactic Nuclei*. University Science Books, Mill Valley, CA
- Phillips J. P., Cuesta L., 1998, *A&AS*, 133, 381
- Phillips J. P., Cuesta L., 1999, *AJ*, 118, 2919
- Phillips J. P., Cuesta L. C., Ramos-Larios G., 2010, *MNRAS*, 409, 881
- Prinja R. K., Barlow M. J., Howarth I. D., 1990, *ApJ*, 361, 607
- Raga A. C., Lora V., Smith N., 2010, *Rev. Mex. Astron. Astrofis.*, 46, 179
- Rathborne J. M., Johnson A. M., Jackson J. M., Shah R. Y., Simon R., 2009, *ApJS*, 182, 131
- Riesgo H., López J. A., 2006, *Rev. Mex. Astron. Astrofis.*, 42, 47
- Rola C., Pelat D., 1994, *A&A*, 287, 676
- Sabbadin F., Minello S., Bianchini A., 1977, *A&A*, 60, 147
- Shi H. M., Hu J. Y., 1999, *A&AS*, 136, 313
- Tenorio-Tagle G., 1979, *A&A*, 71, 59
- Tenorio-Tagle G., Bedjin J. P., 1981, *A&A*, 99, 305
- Tenorio-Tagle G., Beltrametti M., Bodenheimer P., Yorke H. W., 1982, *A&A*, 112, 104
- Weaver R., McCray R., Castor J., Shapiro P., Moore R., 1977, *ApJ*, 218, 377
- Westerhout G., 1958, *Bull. Astron. Inst. Neth.*, 14, 215

This paper has been typeset from a  $\text{\LaTeX}$  file prepared by the author.